Using Loop-Gap Resonators to Characterize the Permeability of Metamaterials at Microwave Frequencies

by

Ava H. Cornell

A THESIS SUBMITTED IN PARTIAL FULFILLMENT OF
THE REQUIREMENTS FOR THE DEGREE OF

BACHELOR OF SCIENCE WITH HONOURS

in

Irving K. Barber Faculty of Science

(Physics)

THE UNIVERSITY OF BRITISH COLUMBIA

(Okanagan)

May 2021

Abstract

A negative-index material (NIM), a metamaterial with simultaneously negative effective permittivity and permeability, was composed from periodic arrays of split-ring resonators (SRRs) and aluminum cut wires. The NIM was loaded into the bore of a loop-gap resonator (LGR) and reflection coefficient measurements were used to characterize its permeability. Unexpectedly, many numerical simulations and experimental measurements have suggested that the imaginary component of the cut wire permeability can be negative which implies power generation rather than dissipation. In this project, the reflection coefficient measurements were fit to a model proposed by Pendry and coworkers and used to determine the resonant frequency, magnetic plasma frequency, and damping constant of the metamaterial's effective permeability. By comparing these parameters with those found for arrays of exclusively SRRs, the presence of cut wires was shown to have almost no effect on the permeability of the NIM when in the presence of a pure magnetic field. In future research, similar analysis could be done for measurements taken when an external source is used to establish a current in the cut wires.

Table of Contents

Appendices

List of Tables

List of Figures

Acknowledgements

First and foremost, I would like to thank Dr. Jake Bobowski for the opportunity to work with him on this project. I cannot adequately express how much I appreciate the support he has given me in writing this thesis, throughout this project, and over the course of my degree. I would also like to thank my family for their encouragement throughout all of my endeavours.

Chapter 1

Introduction

In this thesis we will develop a method to experimentally measure the permeability of metamaterials composed of arrays split-ring resonators (SRRs) and cut wires. In order to do this, we will use loop-gap resonators (LGRs) and employ Pendry *et al.*'s model to characterize these arrays [1].

1.1 Metamaterials

Metamaterials are materials engineered to have electromagnetic properties that are not found in natural materials. Specifically, all naturally-occurring materials have a positive electric permittivity, ε_r, magnetic permeability, μ_r, and refractive index, n. Whereas for metamaterials, at least one of these properties, given by Eqs. (1.1) to (1.3) respectively, is negative [2].

$$\varepsilon_r = \frac{\varepsilon}{\varepsilon_0} \qquad (1.1) \qquad\qquad \mu_r = \frac{\mu}{\mu_0} \qquad (1.2) \qquad\qquad n = \sqrt{\varepsilon_r \mu_r} \qquad (1.3)$$

Note that ε_0, the permittivity of free space, has the approximate value of 8.85×10^{-12} F/m and μ_0, the permeability of free space, has the value $4\pi \times 10^{-7}$ H/m. In this project, we will be focusing on negative index materials (NIMs) which classify a specific type of metamaterial that has a negative index of refraction over part of the electromagnetic spectrum. For this to occur, the permeability and permittivity must be simultaneously negative [3].

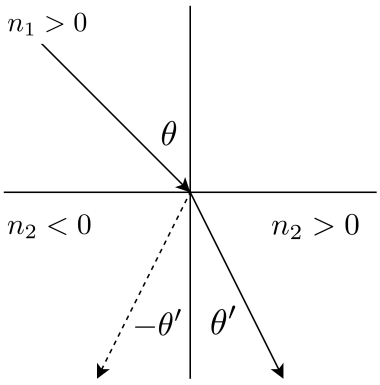

Figure 1.1: An EM wave moving from a conventional material (with $n_1 > 0$) into an NIM ($n_2 < 0$, dashed line) and a material with a positive refractive index ($n_2 > 0$, solid line).

This effect can be further explained by showing an EM wave moving from a conventional material into a NIM compared to when it moves into another conventional material with a positive refractive index, as shown in Fig. 1.1. To analyze this situation, we will follow the work done by V. G. Veselago in his 1968 paper "The Electrodynamics of Substances with Simultaneously Negative Values of ε and μ" [4]. To begin we will define the boundary conditions for the electromagnetic wave as it moves from material 1 into material 2 to be:

$$\vec{E}_1^{\parallel} = \vec{E}_2^{\parallel} \tag{1.4}$$

$$\vec{H}_1^{\parallel} = \vec{H}_2^{\parallel} \tag{1.5}$$

$$\varepsilon_1 E_1^{\perp} = \varepsilon_2 E_2^{\perp} \tag{1.6}$$

$$\mu_1 H_1^{\perp} = \mu_2 H_2^{\perp} \tag{1.7}$$

Here, we have denoted the electric field as $\vec{E}$ and the magnetic field intensity as $\vec{H}$. The superscript $\parallel$ is used to describe the component of the waves that is parallel to the boundary between material 1 and material 2, while $\perp$ describes the component perpendicular to the boundary. Lastly, μ_1 and ε_1 describe the permeability and permittivity of material 1 and μ_2 and ε_2 describe the permeability and permittivity of material 2 [5]. Before we begin our analysis of the effects of μ_2 and ε_2 on these boundary conditions, we will define $\vec{E}$ to be travelling in the plane of the paper. This results in $\vec{H}$ travelling perpendicular to the page, and thus $\vec{H}$ has no component perpendicular to the boundary between material 1 and 2. This yields the trivial result of zero equals zero for the boundary condition denoted by Eq. (1.7).

To begin, we will assume that our EM wave is travelling from material 1 into material 2 which are both defined to have positive permittivity and permeability, but, $\varepsilon_2 > \varepsilon_1$. As Eqs. (1.4) and (1.5) do not depend on permittivity or permeability and Eq. (1.7) has a trivial solution, we are only interested in Eq. (1.6). For these conditions, Eq. (1.6) yields,

$$E_2^{\perp} = \frac{\varepsilon_1}{\varepsilon_2} E_1^{\perp}, \tag{1.8}$$

where, from our initial set-up, we can deduce that $E_2^{\perp} < E_1^{\perp}$. This is consistent with Snell's law, $n_1 \sin\theta = n_2 \sin\theta'$. Now, we can perform a similar analysis for when material 2 is defined to have a negative permeability, μ_2, and permittivity, ε_2, while μ_1 and ε_1 remain positive. Again, we are only interested in analyzing Eq. (1.6), which again yields Eq. (1.8). However, for this scenario $\frac{\varepsilon_1}{\varepsilon_2} < 0$ so $E_2^{\perp}$ is refracted in a different direction and results in a negative angle of refraction. This is illustrated by the dashed line in Fig. 1.1. Therefore, for this material, Snell's law results in $n_1 \sin\theta = n_2 \sin{-\theta'} = -n_2 \sin\theta'$. Thus, for Snell's law to hold, it is required that the refractive index, n_2, is negative for materials with negative permeability, μ_2, and permittivity, ε_2.

In this thesis, we will construct arrays of cut wires as well as arrays of both SRRs and cut wires and characterize their effective relative permeability, μ_r, at microwave frequencies.

In "The Complex Permeability of Split-Ring Resonator Arrays Measured at Microwave Frequencies" S.L. Madsen and J.S. Bobowski, measured the permeability of SRR arrays [6]. Now, we will work to see what effect, if any, that addition of cut wires has to these arrays. Previous numerical simulations and experimental measurements have suggested that the imaginary component of $\mu_r = \mu' - j\mu''$ is negative for arrays of cut wires [7]. This is unexpected as it suggests power gain rather than dissipation in the NIM.

1.1.1 Applications

NIMs have many interesting applications which include the creation of super lenses as well as cloaking devices [2]. Conventional lenses can only focus light on areas equal to or larger than its wavelength squared. Many simulations have suggested that by utilizing NIMs, a super lens could be created that is not limited by wave optics [8]. Additionally, NIMs have been proposed to be able shield an object from view by controlling its EM radiation [9].

1.2 Split-Ring Resonators (SRRs)

For the purposes of this project, we will define SRRs as planar structures with negligible length, composed of two concentric, conducting rings with slits in each, on opposing sides, as shown in Fig. 1.2. In 1999, Pendry *et al.* proposed SRR arrays exhibit a

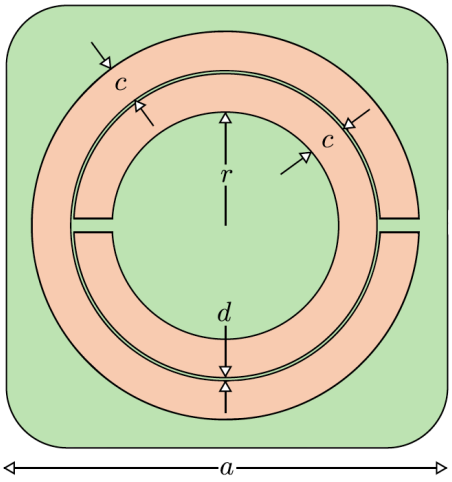

Figure 1.2: Schematic depiction of an SRR with radius, r, ring thickness, c, and distance between conductors, d. Taken from [6].

negative effective permeability just above their resonant frequency [1]. He derived a model for the real, μ', and imaginary, μ'', components of the an SRR arrays effective relative permeability, which are given by:

$$\mu_r = \mu' - j\mu'' \tag{1.9}$$

$$\mu' = 1 - \frac{[1-(\omega_s/\omega_p)^2][1-(\omega_s/\omega)^2]}{[1-(\omega_s/\omega)^2]^2+(\gamma/\omega)^2]} \tag{1.10}$$

$$\mu'' = \frac{(\gamma/\omega)[1-(\omega_s/\omega_p)^2]}{[1-(\omega_s/\omega)^2]^2+(\gamma/\omega)^2}. \tag{1.11}$$

Here, ω_s denotes the SRRs resonant angular frequency, ω_s is the SRRs magnetic plasma angular frequency, and γ is the damping constant, which characterizes the sharpness of the resonance.

1.2.1 Dimensions and Materials

The SRRs used in this project are depicted in Fig. 1.2. They were made by S. L. Madsen and J. S. Bobowski [6]. The SRR itself is secured on FR-4 printed circuit board, shown in green in Fig. 1.2, which has a dielectric constant of about 4.5 at frequency of 1 GHz [10] [6]. The circuit board had thickness $t = 1.54$ mm and side-length $a = 21.0$ mm and the SRR has dimensions $r = 5.56$ mm, $c = 1.91$ mm. $d = 0.15$ mm [6]. Additionally, 2×2 planes of four SRRs were composed on printed circuit board of side-length $2a$ with evenly spaced SRRs in each quadrant.

1.3 Cut Wire Arrays

Arrays of conducting wires are known to have a negative effective permittivity. Maslovski *et al.* derived a model describing the effective permittivity of an array of cut wires under quasi-static conditions [11]. This model considered a infinite periodic array of conducting wires as depicted in Fig. 1.3. It was assumed that in these arrays of wires, only EM plane waves in the fundamental Floquet mode can propagate [12]. This derivation resulted in the permittivity of the array being defined as,

$$\overline{\overline{\varepsilon}} = \varepsilon_0 \left(\overline{\overline{I}} - \frac{2\pi \vec{z_0}\vec{z_0}}{(ka)^2 \log(\frac{a^2}{4r_0(a-r_0)})} \right), \tag{1.12}$$

where $\overline{\overline{I}}$ is the identity tensor, and the wave number, k, is given by $\omega\sqrt{\epsilon_0\mu_0}$, where ω is the angular frequency. Moreover, $\vec{z_0}$ describes the unit vector in the z direction. Thus, the vector product of z_0 with itself results in a matrix which isolates the electric field travelling in the z direction, which, in this model, is along the axis of the cut wire array. The cut-off wavelength, which restricts the modes of the plane wave travelling through the cut wire array to the Floquet mode, is therefore given by,

$$\lambda_0 = a\sqrt{(2\pi)\log\left(\frac{a^2}{4r_0(a-r_0)}\right)}. \tag{1.13}$$

This result, which only pertains to ideally conducting wires, was then extended to incor-

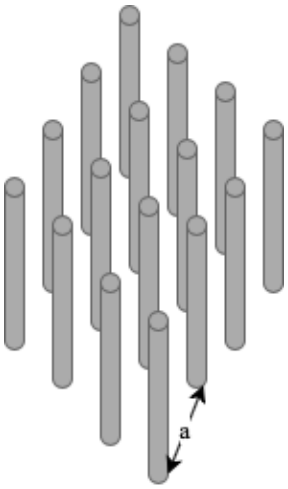

Figure 1.3: An infinite periodic array of cut wires. Array has period a and wires have radius r_0. Figure modelled after Fig. 1.4(a) in [13].

porate lossy and loaded wires [11]. These wires were described by having an additional effective surface impedance,

$$Z_s = \frac{1+j}{\sqrt{2}}\sqrt{\frac{\omega\mu_0}{\sigma}}, \tag{1.14}$$

where σ is the metal conductivity. This impedance is added with the impedance of the arrays inductance to yield the complex permittivity,

$$\overline{\overline{\varepsilon}} = \varepsilon_0\left(\overline{\overline{I}} - \frac{2\pi\vec{z_0}\vec{z_0}}{(ka)^2\log(\frac{a^2}{4r_0(a-r_0)}) - jka\frac{a}{r_0}\frac{Z_s}{\eta}}\right), \tag{1.15}$$

where η, the free-space impedance is given by $\sqrt{\mu_0/\varepsilon_0}$. Overall, similarly to effective relative permeability, effective relative permittivity can be expressed conventionally as a complex value,

$$\varepsilon_r = \varepsilon' - j\varepsilon'', \tag{1.16}$$

where ε' is the real component of permittivity and ε'' is the imaginary component of permittivity when losses are considered. Unlike the permeability of SRR arrays, which is only negative right above its resonance frequency, the permittivity of cut wire arrays can be negative over a broad range of frequencies. This is further explored in Chapters 5.1 and 5.2.

1.4 Loop-Gap Resonators (LGRs)

In order to measure the permeability of our arrays of both cut wires and SRRs, loop-gap resonators (LGRs) will be used. An LGR is composed of a long, hollow bore made of conducting material with a gap down the entire length of the bore and a coupling loop suspended in one end. The cross-section of a one-loop-one-gap LGR is shown in Fig. 1.4(a), while the actual resonator used is pictured in Fig. 1.4(b).

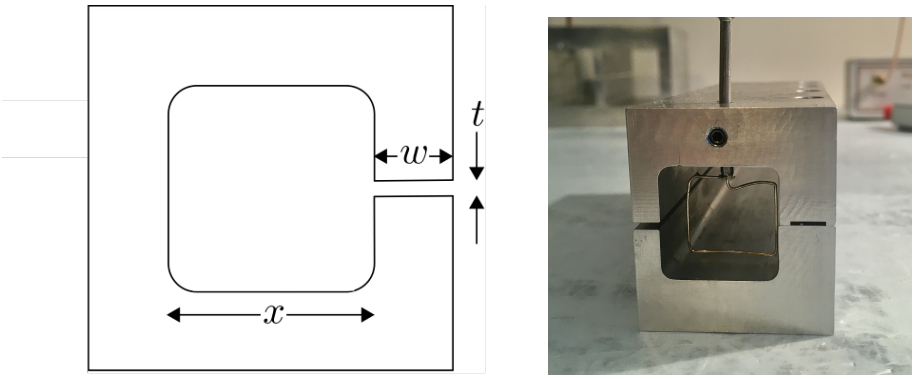

(a) Schematic. Figure modified from [14].

(b) LGR used for measurements.

Figure 1.4: The cross-section of a one-loop-one-gap resonator with gap thickness t, gap width w, and bore side-length x.

Figure 1.4 shows that the corners of the LGR's bore are rounded which was done to avoid large current densities that would be expected at sharp corners [6]. However, the side-length of the bore is still given as x and the cross-sectional area is approximated to be x^2. LGRs is can be easily modelled as LRC circuits. An LRC circuit, such as the one shown in Fig. 1.5, is a simple circuit with an inductor, capacitor, and a resistor in series. Typically, LGR's are cylindrical with a circular cross-section of inner radius, r_0. The shell of the LGR acts as a single turn inductor with inductance, $L \approx \frac{\mu_0 \pi {r_0}^2}{l}$, where the cross-sectional area of the circular bore is given by $\pi {r_0}^2$ and its length is denoted l. The capacitance is given by $C_0 \approx \frac{\varepsilon_0 w l}{t}$ and the resistance is $R_0 \approx \frac{2\rho\pi r_0}{l\delta_0}$, where the circumference of the bore in $2\pi r_0$ and δ is the skin depth of the material that the LGR is made from [15]. Skin depth is a frequency dependent quantitative measure of how deep the AC current flowing in the resonator penetrates into its surface [15]. Specifically, δ_0, denotes the skin depth of the resonator at its resonant frequency [14]. These parameters can be modified for our rectangular LGR with a square cross-section by substituting in x^2 as the cross-sectional area and $4x$ as the bore's inner perimeter.

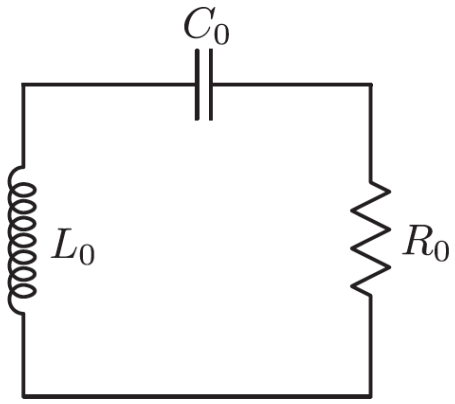

Figure 1.5: The equivalent circuit model of an LGR bore. Figure modified from [14].

The approximate inductance can then be represented as,

$$L_0 \approx \frac{\mu_0 x^2}{l}. \tag{1.17}$$

The gap of the LGR has the same dimensions, so it provides the same capacitance of,

$$C_0 \approx \frac{\varepsilon_0 w l}{t}. \tag{1.18}$$

Lastly, the effective resistance of the LGR at its resonance frequency, ω_0, is denoted,

$$R_0 \approx \frac{4\rho x}{l\delta_0}. \tag{1.19}$$

We can calculate the skin depth of an LGR using,

$$\delta = \sqrt{\frac{2\rho}{\mu_0 \omega}}, \tag{1.20}$$

where ρ is the resistivity of the material the LGR is composed of [15]. The LGRs used in this project are made of aluminum which has resistivity $\rho = 2.82\times10^{-8}$ Ωm [16]. From these parameters, the resonance frequency of the LGR is estimated to be,

$$f_0 = \frac{1}{2\pi\sqrt{LC}}, \tag{1.21}$$

where L and C are given by L_0 and C_0 for an empty LGR. This logic can also be extended to a two-loop-one-gap LGR. However, while the capacitance of the LGR is still determined by the dimensions of the gap, the inductance and resistance are independent for each bore. These larger LGRs were used to accommodate large 2×2 arrays of SRRs and cut wires.

1.4.1 Dimensions

The one-loop-one-gap LGR we used, as shown in Figs. 1.4(a) and (b), had dimensions $l = 112$ mm, $x = 21.6$ mm, $w = 5.0$ mm, and $t = 1.3$ mm [6]. Using these dimensions in conjunction with Eqs. (1.17), (1.18), and (1.21), we estimate the resonance frequency of the empty loop gap resonator to be 1 GHz. Additionally, a two-loop-one-gap resonator, as shown in Figs. 1.6(a) and (b), was used. It had dimensions $l = 112$ mm, $x = 42.7$ mm, $w = 5.0$ mm, and $t = 2.0$ mm [6]. As the bore of this resonator is larger, its inductance will increase relative to the one-loop-one-gap resonator. This, in turn, will lower the resonance frequency. In order to counteract this change, the capacitance of the LGR was increased by increasing the gap thickness, t, with respect to the one-loop-one-gap resonator. This yields an expected resonance frequency of approximately 0.7 GHz for the empty two-loop-one-gap LGR.

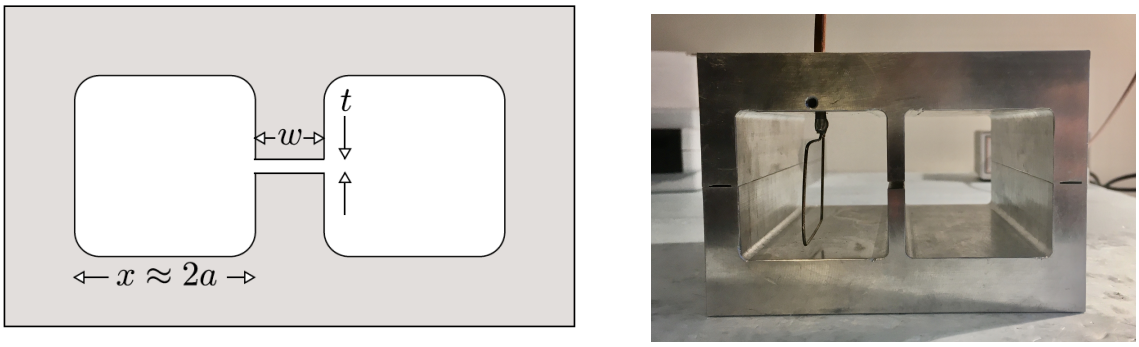

(a) Schematic. Taken from [6].

(b) LGR used for measurements.

Figure 1.6: Two-loop-one-gap resonator with gap thickness, t, and gap width, w.

Chapter 2

Measurement Methods

In order to collect data, a vector-network analyzer (VNA) was used. Specifically, the DG8SAQ VNA 3E from SDR-Kits. This VNA is powered from a PC USB-bus and covers frequencies from 1 kHz to 1.3 GHz. The VNA, which was connected to the LGR's coupling loop using an SMA cable, allowed us to both introduce and extract signals from our LGR. Specifically, we will be interested in characterizing the reflected signal. To do this, we will measure the coefficient of the reflected signal, S_{11}, from our LGR's coupling loop.

Before we could take these measurements, the system had to be calibrated. To do this, we used the Magi-Cal device. Essentially, once the settings for this automatic calibration system were loaded into data collection software, the Magi-Cal device was connected to the LGR's coupling loop using an SMA cable. From here, the calibration was run. As for this portion of data collection we were only interested in the reflected signal, the calibration was set to only run through an open circuit, a short circuit, and a circuit with a 50 Ω load. Additionally, the audio settings of the VNA were adjusted to collect forty samples per IF period, three pre-samples, and 3 post-samples. This resulted in the desired sinusoidal signal being delivered to the coupling loop. Once the VNA was set up, we were able to acquire S_{11} sweeps over various ranges of microwave frequencies.

The VNA collected S_{11} data on a logarithmic decibel scale. In order to analyze the data, we converted it to a linear scale using,

$$|S_{11}|_{\text{lin}} = 10^{|S_{11}|_{\text{dB}}/20}. \tag{2.1}$$

In Eq. (2.1), the absolute value bars indicate that we are only concerned with the magnitude of the S_{11} signal. Additionally, the factor of twenty in the exponent is due to the $|S_{11}|_{\text{lin}}$ being defined in terms of a voltage ratio instead of a power ratio as shown by Eqs. (2.2) and (2.3).

$$|S_{11}|_{\text{dB}} = 10\log\left(\frac{V_2}{V_1}\right)^2 \tag{2.2}$$

$$|S_{11}|_{\text{lin}} = \frac{V_2}{V_1} \tag{2.3}$$

Here, V_1 denotes the voltage supplied to the coupling loop and V_2 denotes the reflected voltage. Thus, as the voltage ratio is equivalent to the square root of the power ratio, there is an extra factor of one-half in the exponent as we convert from the decibel scale.

Chapter 3

Modelling $|S_{11}|$ of An Empty LGR

To model $|S_{11,\mathrm{e}}|$ we must calculate the effective impedance of the empty LGR, Z_e, and then exploit the characteristics of transmission lines to determine the reflection coefficient.

3.1 The Effective Impedance of a Loop Gap Resonator (LGR)

In order to find the effective impedance of a one-loop-one-gap resonator inductively coupled to a coupling loop of inductance L_1, its equivalent circuit model, as depicted in Fig. 3.1, was analyzed.

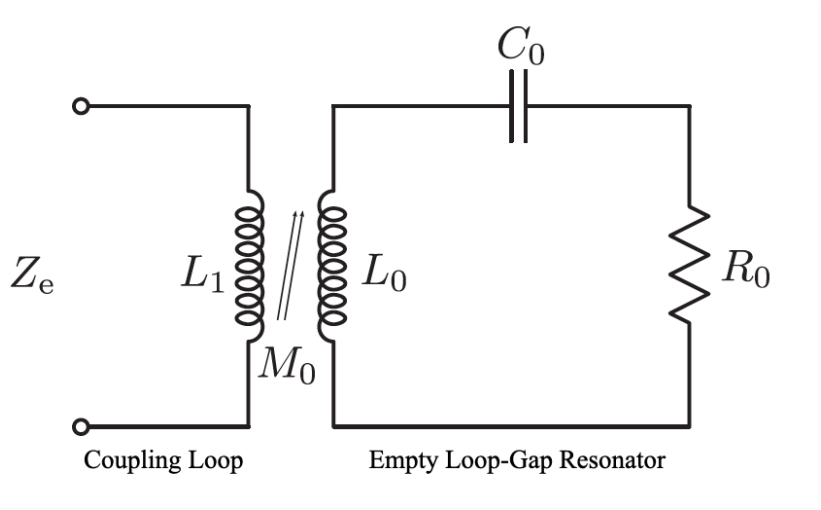

Figure 3.1: The equivalent circuit model of an LGR inductively coupled to a coupling loop of inductance, L_1. Figure modified from [14].

In Fig. 3.1, L_1 is the effective inductance of the coupling loop, which is assumed to have no losses. L_0 denotes the self inductance of the LGR which is defined as the ratio of magnetic flux to the opposing current in a loop. C_0 is the capacitance of the LGR gap and R_0 is its effective resistance at its resonance frequency. More generally, the effective resistance of the LGR at all frequencies can be denoted R. Lastly, M_0 represents the mutual inductance between L_1 and L_0 and is given by $k\sqrt{L_0 L_1}$, where k is a coupling coefficient whose value is between zero and one [17].

In order to analyze this circuit, Kirchhoff's voltage law is applied. This law states that the sum of the potential differences around a loop equals zero [18]. A voltage is applied to the coupling loop from the VNA which drives a current, i_1, across the coupling loop. This, in turn, induces an emf through the resonator bore resulting in a second current, i_2, in the LGR. Additionally, the impedance of the LGR's capacitance is defined as $Z_{\mathrm{C}_0} = 1/j\omega C_0$ and the impedance of the LGR's inductance is defined as $Z_{\mathrm{L}_0} = j\omega L_0$. Applying Kirchhoff's voltage law to the coupling loop we obtain

$$V_1 = j\omega L_1 i_1 + j\omega M_0 i_2, \tag{3.1}$$

where V_1 is the voltage applied to the coupling loop. Now, analyzing the circuit loop of the LGR we obtain,

$$0 = j\omega M_0 i_1 - \frac{j i_2}{\omega C_0} + i_2 R + j\omega L_0 i_2. \tag{3.2}$$

Solving Eq. (3.2) for i_2 we obtain,

$$i_2 = i_1 \frac{-j\omega M_0}{R + j(\omega L_0 - \frac{1}{\omega C_0})}. \tag{3.3}$$

The effective impedance is defined as $Z_{\mathrm{e}} = V_1/i_1$. Therefore, by combining Eqs. (3.1) and (3.3) and factoring out and dividing by i_1 we find,

$$Z_e = \frac{V_1}{i_1} = j\omega L_1 + \frac{\omega^3 M_0^2 C_0}{R\omega C_0 + j(\omega^2 L_0 C_0 - 1)}. \tag{3.4}$$

By multiplying by the complex conjugate of the denominator in Eq. (3.4), the imaginary and real components of Z_{e} are separated where $Z_{\mathrm{e}} = R_{\mathrm{e}} + jX_{\mathrm{e}}$. The real component of the effective impedance is,

$$R_{\mathrm{e}} = \frac{R\omega^2 M_0^2}{R^2 + (\omega L_0 - \frac{1}{\omega C_0})^2}, \tag{3.5}$$

and the imaginary component of the effective impedance is,

$$X_{\mathrm{e}} = \omega L_1 - \omega^2 M_0^2 \frac{\omega L_0 - \frac{1}{\omega C_0}}{R^2 + (\omega L_0 - \frac{1}{\omega C_0})^2}. \tag{3.6}$$

Now, to obtain the desired form of Z_{e}, we must express Eqs. (3.5) and (3.6) in terms of ω_0, Q_0, and R_0 by re-expressing L_0 and C_0 as $L_0 = Q_0 R_0/\omega_0$ and $C_0 = 1/\omega_0 Q_0 R_0$. Additionally, we can write R in terms of R_0 by analyzing the skin depth, δ, of the resonator. The skin depth, denoted by Eq. (1.20), is a quantitative measure of how deeply the AC current flowing in the resonator penetrates the surface. Thus, the resistance of the LGR can be represented by,

$$R = \frac{4\rho x}{l\delta}, \tag{3.7}$$

where l is the length of the resonator, x is the side length, and ρ is the resistivity of the material [15]. Now, by combining Eqs. (1.20) and (3.7) and defining $R_0 = 2\sqrt{2\rho\mu_0\omega_0}(x/l)$, where μ_0 is the permeability of free space, we obtain $R = R_0\sqrt{\omega/\omega_0}$ [14]. By implementing these changes, we obtain the real and imaginary components of Z_e shown in Eqs. (3.8) and (3.9), respectively.

$$R_\mathrm{e} = \frac{[(\omega M_0)^2/R_0]\sqrt{\omega/\omega_0}}{(\omega/\omega_0) + Q_0^2[(\omega/\omega_0) - (\omega_0/\omega)]^2} \tag{3.8}$$

$$X_\mathrm{e} = \omega L_1 - \frac{[(\omega M_0)^2/R_0]Q_0[(\omega/\omega_0) - (\omega_0/\omega)]}{(\omega/\omega_0) + Q_0^2[(\omega/\omega_0) - (\omega_0/\omega)]^2} \tag{3.9}$$

3.2 Modelling $|S_{11,\mathrm{e}}|$ of an Inductively-Coupled LGR

Now that we have determined the effective impedance of an empty LGR, Z_e, we can consider the characteristics of transmission lines to model the magnitude of the reflected signal, $|S_{11,\mathrm{e}}|$. The LGR is inductively-coupled to a coupling loop connected to a coaxial cable with characteristic impedance Z_0. In order to find the reflection coefficient using Z_e and Z_0 we must exploit the result,

$$S_{11,\mathrm{e}} = \frac{Z_\mathrm{e} - Z_0}{Z_\mathrm{e} + Z_0}, \tag{3.10}$$

where $Z_\mathrm{e} = R_\mathrm{e} + jX_\mathrm{e}$ and, the characteristic impedance, Z_0, of our transmission line is 50 Ω [19]. Combining this expression for Z_e with Eq. (3.10) and multiplying by the complex conjugate, we obtain:

$$S_{11,e} = \frac{R_\mathrm{e}^2 + X_\mathrm{e}^2 - Z_0^2}{(R_\mathrm{e} + Z_0)^2 + X_\mathrm{e}^2} + j\frac{2Z_0X_\mathrm{e}}{(R_\mathrm{e} + Z_0)^2 + X_\mathrm{e}^2}. \tag{3.11}$$

To solve for the magnitude of the reflected signal $|S_{11,\mathrm{e}}|$, we must multiply Eq. (3.11) by the complex conjugate and square root the result. This results in the following expression for the magnitude of the reflection coefficient for an inductively-coupled empty LGR:

$$|S_{11,\mathrm{e}}| = \frac{\sqrt{[(|Z_\mathrm{e}|^2/Z_0^2) - 1]^2 + [2(X_\mathrm{e}/Z_0)]^2}}{[(|Z_\mathrm{e}|^2/Z_0^2) + 1] + 2(R_\mathrm{e}/Z_0)}, \tag{3.12}$$

where $|Z_\mathrm{e}|^2 = R_\mathrm{e}^2 + X_\mathrm{e}^2$.

3.3 Plotting $|S_{11,\mathrm{e}}|$ for Varying Coupling Constants

Using Eq. (3.12) in conjunction with Eqs. (3.8) and (3.9) we can plot $|S_{11,\mathrm{e}}|$ as a function of frequency for different values of mutual inductance, M_0. Here, ${M_0}^2/R_0$ is set equal to $k^2\times(0.1\mathrm{nH}^2/\mathrm{m}\Omega)$, where k is the coupling coefficient. Additionally, we will use test

values of $\omega_0 = 2\pi\times(1\text{ GHz})$, $Q_0 = 500$, $L_1 = 12$ nH, and $Z_0 = 50\ \Omega$. To vary the mutual inductance, M_0, $|S_{11,e}|$ is plotted as a function of frequency for $k = 0.1$, 0.2, 0.3, 0.4, and 0.5. The resulting plots are shown in Fig. 3.2.

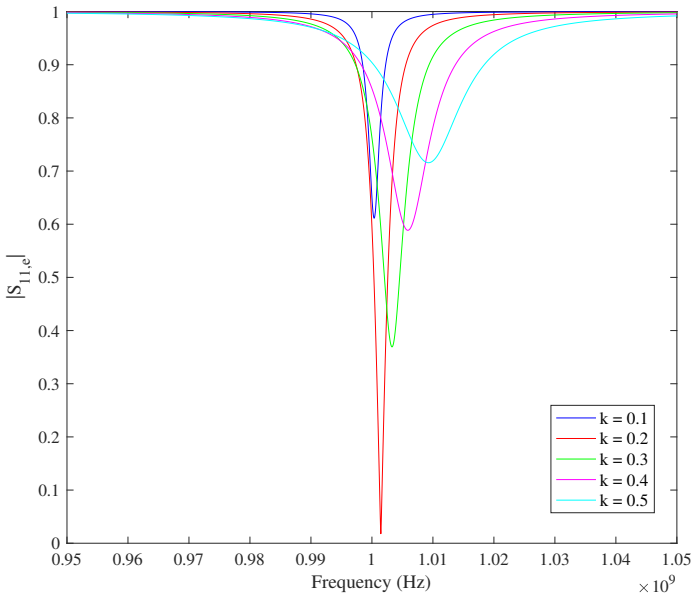

Figure 3.2: $|S_{11,e}|$ plotted as a function of frequency for $k = 0.1$, 0.2, 0.3, 0.4, and 0.5.

As shown in Fig. 3.2, when $k = 0.2$, $|S_{11,e}|$ approaches a value very close to zero at its resonance peak. For critically coupled systems, the maximum signal is transferred from the coupling loop to the LGR, which means Z_e is equal to Z_0 as shown by Eq. (3.10). Therefore, $|S_{11,e}|$ is equal to zero meaning the LGR and coupling loop are critically coupled when $k = 0.2$. Thus, when $k < 0.2$, the LGR is undercoupled. The plot resulting from an undercoupled mutual inductance, for example when $k = 0.1$, is shifted left and has a higher $|S_{11,e}|$ value at resonance. Lastly, when $k > 0.2$, the LGR is overcoupled. The plot resulting from an overcoupled mutual inductance, as shown in Fig. 3.2 when $k = 0.3$, 0.4, and 0.5, is less sharp, shifted right, and has a higher $|S_{11,e}|$ value at resonance [20].

3.4 Experimentally Determining $|S_{11,e}|$ for Varying Coupling Constants

$|S_{11,e}|$ as a function of frequency was measured using the two-loop-one-gap resonator shown in Fig. 1.6. In order to change the coupling constant k, the orientation of the coupling loop was tuned. To find the orientation that resulted in critical coupling, the coupling loop was tuned until $|S_{11,e}|$ approached zero. From here, it was adjusted until a characteristic undercoupled peak was seen, and further adjusted until a characteristic

overcoupled peak was seen. The data collected was then linearized using Eq. (2.1) and plotted as shown in Fig. 3.3.

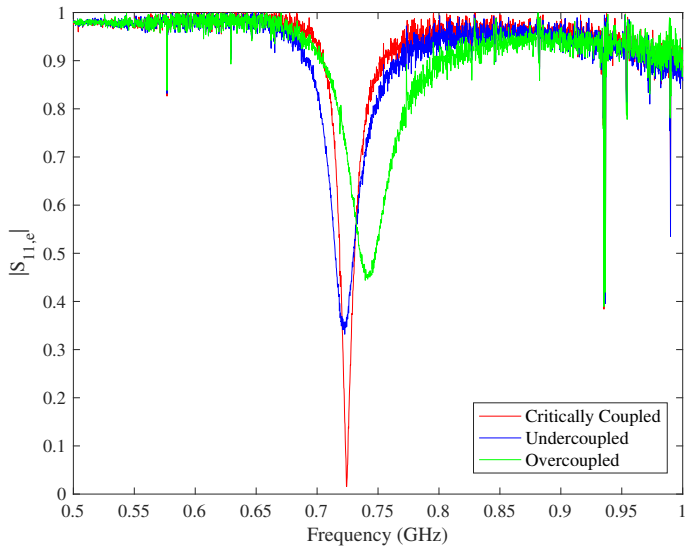

Figure 3.3: $|S_{11,e}|$ plotted as a function of frequency for two-loop-one-gap resonator for various coupling loop orientations.

Comparing Fig. 3.2 and Fig. 3.3, we can see that in both figures the plots produced when the LGR and coupling loop are critically coupled approach zero at their resonance frequencies. On the other hand, the undercoupled and overcoupled plots have greater values of $|S_{11,e}|$ for their resonance peaks. As expected, as shown in Fig. 3.3, the undercoupled plot has a slightly lower resonance frequency and the overcoupled plot has a slightly higher resonance frequency and less defined peak. Additionally, it is important to note that the two-loop-one-gap LGR's resonant frequency, f_0, was estimated to be approximately 0.7 GHz. Therefore, while the the model for the one-loop-one-gap resonator shown in Fig. 3.2 shows resonances occurring at $\sim$ 1 GHz, it is expected that f_0 for measurements taken using the two-loop-one-gap resonator will be closer to 0.7 GHz, as observed.

Chapter 4

Permeability of SRR Arrays

4.1 Modelling Permeability of SRR Arrays

In order to analyze the permeability of SRR arrays, we will be using Pendry *et al.*'s model as given in Eqs. (1.9) to (1.11) [1]. Eqs. (1.10) and (1.11) can be re-written in terms of frequency by substituting in $\omega = 2\pi f$. This yields,

$$\mu' = 1 - \frac{[1 - (f_s/f_p)^2][1 - (f_s/f)^2]}{[1 - (f_s/f)^2]^2 + [\gamma/(2\pi f)]^2} \tag{4.1}$$

and

$$\mu'' = \frac{[\gamma/(2\pi f)][1 - (f_s/f_p)^2]}{[1 - (f_s/f)^2]^2 + [\gamma/(2\pi f)]^2}, \tag{4.2}$$

where f_s is the resonant frequency, f_p is the plasma frequency, and γ is the damping constant [1]. Now, as our SRR arrays are expected to have resonance frequencies of approximately 1 GHz, we can set $f_\mathrm{s} = 1$ GHz, from here we set f_p equal to 1.05 GHz and $\gamma/(2\pi)$ to 10 MHz. Using these test values, we can plot μ' and μ'' as a function of frequency. The obtained curves are plotted in Fig. 4.1.

As depicted in Fig. 4.1, μ' is negative just above its resonance frequency, f_s, until it crosses back over zero at its plasma frequency, f_p. Additionally, μ'' peaks at f_s before returning to zero at f_p. An important feature of this model is that μ'' will be greater than or equal to zero as long as $f_\mathrm{p} > f_\mathrm{s}$. This is expected as a positive μ'' implies power dissipation, which is expected as a signal is supplied and reflected from the metamaterial.

4.2 The Effective Impedance of an LGR Filled with Magnetic Material

As we load SRRs with a complex effective permeability into the bore of an LGR, the relative effective permeability of the LGRs bore will change. We must account for this when we find the impedance of the coupled LGR. To do this, we will complete a similar analysis as shown in Chapter 3.1, but, this time, we will account for the magnetic material filling the LGRs bore. To begin, we must analyze the equivalent circuit model shown in Fig. 4.2.

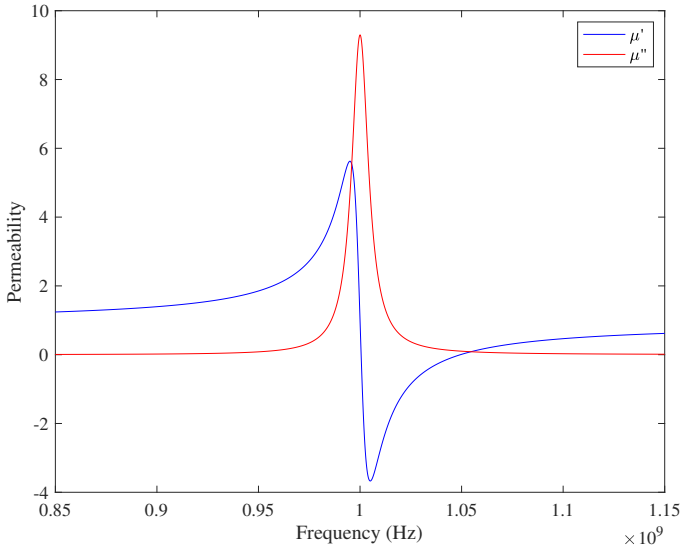

Figure 4.1: The real, μ', and imaginary, μ'', components of the SRR relative permeability plotted as a function of frequency when $f_{\mathrm{p}} = 1.05$ GHz, $f_{\mathrm{s}} = 1$ GHz, and $\gamma/(2\pi) = 10$ MHz.

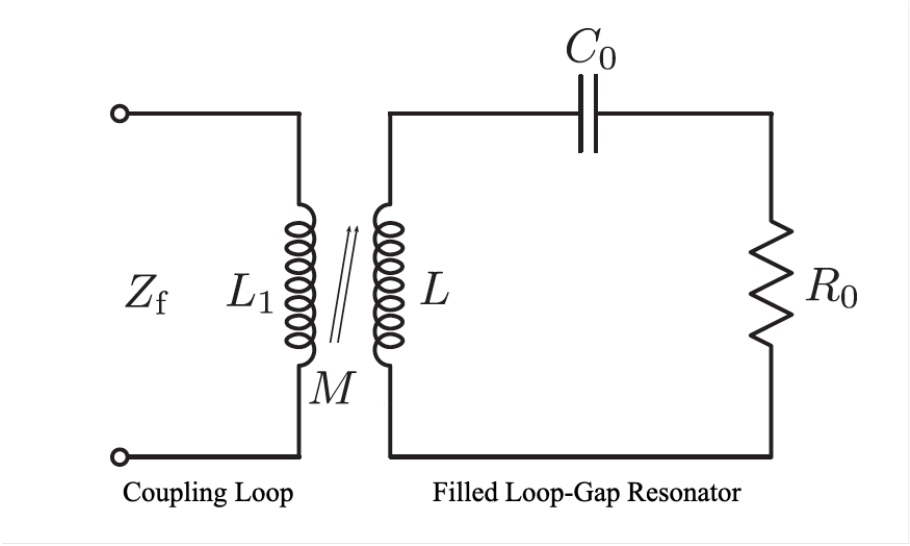

Figure 4.2: The equivalent circuit model of an filled LGR inductively coupled to coupling loop of inductance, L_1. Figure modified from [14].

L_1 denotes the inductance of the coupling loop which is inductively coupled to the LGR, which now has inductance L. For this derivation we will assume the bore of the LGR is filled with a magnetic material having relative permeability $\mu_{\mathrm{r}} = \mu' - j\mu''$. This causes the inductance of the LGR to go from $L = L_0$ to $L = (\mu' - j\mu'')L_0$. Again, the effective capacitance and resistance of the LGR are denoted as C_0 and R_0, respectively. Lastly, the mutual inductance between the coupling loop and the resonator is denoted M. For

an empty LGR bore, the mutual inductance was given by $M_0 = k\sqrt{L_0 L_1}$. Now, however, as the inductance of the bore is being multiplied by μ_r, the mutual inductance becomes $M = k\sqrt{\mu_r L_0 L_1}$. From this, we can make use of the result $M^2 = k^2 \mu_\mathrm{r} L_0 L_1$. Lastly, recall that the resistance of the LGR bore has frequency dependence given by $R = R_0\sqrt{\omega/\omega_0}$.

Similarly to the circuit analysis used to determine the effective impedance of a coupling loop inductively coupled to an empty LGR, Kirchhoff's voltage law will be exploited in this problem [17]. Again, there is a current i_1 in the coupling loop, and thus, by Faraday's Law, a current i_2 is induced in the LGR. Applying Kirchhoff's voltage law to the coupling loop we obtain

$$V_1 = j\omega L_1 i_1 + j\omega M i_2, \tag{4.3}$$

where V_1 is the voltage applied to the coupling loop. Now, analyzing the circuit loop of the LGR we obtain,

$$0 = j\omega M i_1 - \frac{j i_2}{\omega C_0} + i_2 R + j\omega \mu' L_0 i_2 + \omega \mu'' L_0 i_2. \tag{4.4}$$

Solving Eq. (4.4) for i_2 we obtain,

$$i_2 = \frac{-j\omega M}{R + \omega\mu'' L_0 + j(\omega\mu' L_0 - \frac{1}{\omega C_0})} i_1. \tag{4.5}$$

The effective impedance is defined as $Z_\mathrm{f} = V_1/i_1$. Therefore, in order to solve for Z_f we can combine Eqs. (4.3) and (4.5) and factor out i_1 as follows,

$$Z_f = j\omega L_1 + \frac{\omega^3 M^2 C_0}{R\omega C_0 + \omega^2 C_0 \mu'' L_0 + j(\omega^2 \mu' L_0 C_0 - 1)}. \tag{4.6}$$

Now, in order to remove the imaginary term of Z_f from the denominator of the equation, we must multiply the numerator and denominator of Eq. (4.6) by the complex conjugate of the denominator. From this, we obtain,

$$Z_f = j\omega L_1 + \omega^3 M^2 C_0 \frac{R\omega C_0 + \omega^2 C_0 \mu'' L_0 - j(\omega^2 \mu' L_0 C_0 - 1)}{(R\omega C_0 + \omega^2 C_0 \mu'' L_0)^2 + (\omega^2 \mu' L_0 C_0 - 1)^2}. \tag{4.7}$$

We can now utilize the result, $M^2 = k^2 \mu_\mathrm{r} L_0 L_1$ which, as $\mu_\mathrm{r} = \mu' - j\mu''$, can be written as $M^2 = k^2(\mu' - j\mu'')L_0 L_1$. Using the result in Eq. (4.7), and separating the effective impedance as $Z_\mathrm{f} = R_\mathrm{f} + \mathrm{j}X_\mathrm{f}$ we obtain,

$$R_f = \frac{\omega^2 k^2 L_0 L_1 (\mu' R\omega C_0 + \mu'')}{(R\sqrt{\omega C_0} + \sqrt{\omega^3 C_0}\mu'' L_0)^2 + (\sqrt{\omega^3 C_0}\mu' L_0 - \frac{1}{\sqrt{\omega C_0}})^2}, \tag{4.8}$$

which denotes the real component of the effective impedance, and,

$$X_f = \omega L_1 - \frac{\omega^2 k^2 L_0 L_1[\mu''(R\omega C_0 + \omega^2 C_0 \mu'' L) + \mu'(\omega^2 \mu' L_0 C_0 - 1)]}{(R\sqrt{\omega C_0} + \sqrt{\omega^3 C_0}\mu'' L_0)^2 + (\sqrt{\omega^3 C_0}\mu' L_0 - \frac{1}{\sqrt{\omega C_0}})^2}, \tag{4.9}$$

which denotes the imaginary component of the effective impedance. Finally, to obtain the desired form, we must express Eqs. (4.8) and (4.9) in terms of ω_0, Q_0, and R_0 by re-expressing L_0 and C_0 as $L_0 = Q_0 R_0/\omega_0$, $C_0 = 1/\omega_0 Q_0 R_0$, and $R = R_0\sqrt{\omega/\omega_0}$. These substitutions allow us to obtain the desired form of the real and imaginary components of Z_{f} in Eqs. (4.10) and (4.11), respectively.

$$R_f = \frac{\omega L_1(\omega/\omega_0)k^2[\frac{\mu'}{Q_0}\sqrt{\omega/\omega_0} + \mu''(\omega_0/\omega)]}{[\frac{1}{Q_0}\sqrt{\omega/\omega_0} + \mu''(\omega/\omega_0)]^2 + [\mu'(\omega/\omega_0) - (\omega_0/\omega)]^2} \tag{4.10}$$

$$X_f = \omega L_1 \left(1 - \frac{(\omega/\omega_0)k^2[\mu''[\frac{1}{Q_0}\sqrt{\omega/\omega_0} + \mu''(\omega/\omega_0)] + \mu'[\mu'(\omega/\omega_0) - (\omega_0/\omega)]]}{[\frac{1}{Q_0}\sqrt{\omega/\omega_0} + \mu''(\omega/\omega_0)]^2 + [\mu'(\omega/\omega_0) - (\omega_0/\omega)]^2}\right) \tag{4.11}$$

4.3 Plotting $|S_{11,\mathrm{f}}|$

Equation (3.12) models the magnitude of the reflection coefficient of the signal from an inductively coupled empty LGR. This model can be expanded to include measurements in which the LGR bore is filled with magnetic material. This changes the notation slightly to,

$$|S_{11,\mathrm{e/f}}| = \frac{\sqrt{[(|Z_{\mathrm{e/f}}|^2/Z_0^2) - 1]^2 + [2(X_{\mathrm{e/f}}/Z_0)]^2}}{[(|Z_{\mathrm{e/f}}|^2/Z_0^2) + 1] + 2(R_{\mathrm{e/f}}/Z_0)}, \tag{4.12}$$

where $|Z_{\mathrm{e/f}}|^2 = R_{\mathrm{e/f}}^2 + X_{\mathrm{e/f}}^2$ and Z_0 is still the characteristic impedance of the transmission line. Therefore, using this equation in conjunction with Eqs. (4.10) and (4.11) we can plot the reflected signal of an inductively coupled LGR, $|S_{11,\mathrm{e/f}}|$, as a function of frequency. In order to do this, we will use the following parameters $f_0 = 1$ GHz, $Q_0 = 500$, $L_1 = 12$ nH, and $Z_0 = 50\ \Omega$, and $k = 0.065$. Also noting that ω, the angular frequency, is defined as $2\pi f$. By defining these fixed values while varying μ' and μ'', we were able to explore the effect that varying the real and imaginary components of the permeability of the magnetic material filling the resonator's bore will have on the resonance peaks.

Initially, values of $\mu' = 1$ and $\mu'' = 0$ were plotted. This curve corresponds to the near-critical coupling of an LGR with an empty bore and is displayed in blue in Fig. 4.3. Next, values of $\mu' = 1.1$ and $\mu'' = 0$ were plotted. The resulting curve is shown in red in Fig. 4.3. As shown, when μ' is increased above 1, the resonant frequency is lowered by a factor equal to $\sqrt{1/\mu'}$. Lastly, values of $\mu' = 1$ and $\mu'' = 0.01$ were plotted. This result is shown in cyan in Fig. 4.3 and illustrates that when $\mu'' > 0$, the produced curve is much broader and the resonance is no longer critically coupled.

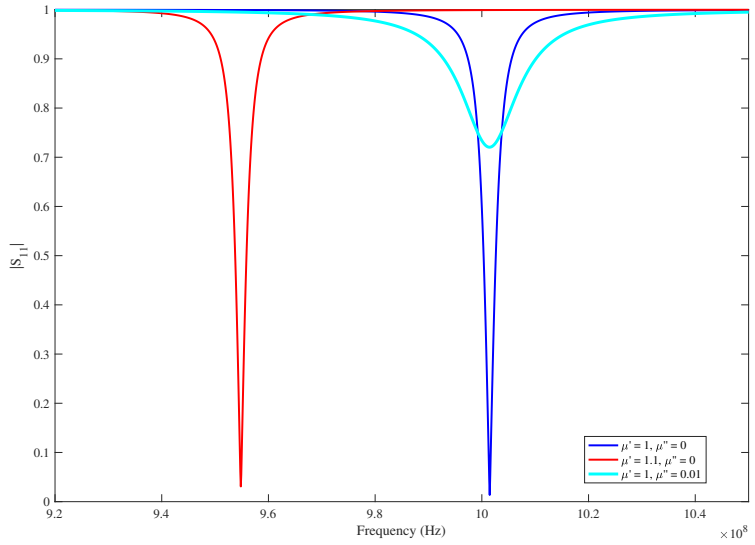

Figure 4.3: $|S_{11,f}|$ plotted as a function of frequency for various permeability values.

4.4 Plotting $|S_{11,f}|$ for Frequency Dependent Permeability

We will also explore the effect the frequency dependent permeability given in Eqs. (4.1) and (4.2) has on the magnitude of the reflection coefficient, $|S_{11,f}|$. In order to do this, we will again plot Eq. (4.12) in conjunction with Eqs. (4.10) and (4.11). However, this time, the real, μ', and imaginary, μ'', components of the relative permeability will be defined by Eqs. (4.1) and (4.2), thus making these values frequency dependent. Similarly to in the plots shown in Figs. 4.1 and 4.3, the following parameters are set: $f_0 = 1$ GHz, $Q_0 = 500$, $L_1 = 12$ nH, and $Z_0 = 50\ \Omega$, $k = 0.065$, and $f_s = 1$ GHz. This time we will be varying f_p and γ to explore the effect they have on the produced resonance curves. Using the outlined values and equations, $|S_{11,f}|$ is plotted as a function of frequency and displayed in Fig. 4.4.

As expected, a double resonance is seen. $|S_{11,f}|$ was originally plotted with $f_p = 1.05$ GHz and $\gamma/(2\pi) = 10$ MHz. These values were then varied to explore their effect on the produced resonance curves. As shown by the red curve, when f_p was decreased to 1.03 MHz, the double resonance peaks shifted closer together. Additionally, the primary resonance peak, while still higher in magnitude than the secondary peak, decreased in magnitude. Moreover, the secondary peak increased in magnitude. Then, as shown by the magenta curve, when f_p was increased to 1.07 MHz, the double resonance peaks shifted further apart and the primary peak increased in magnitude while the secondary peak decreased in magnitude. Next, the damping constant, γ, was varied while f_p stayed constant at 1.05 GHz. As expected, when γ was decreased, as illustrated by the cyan curve, the

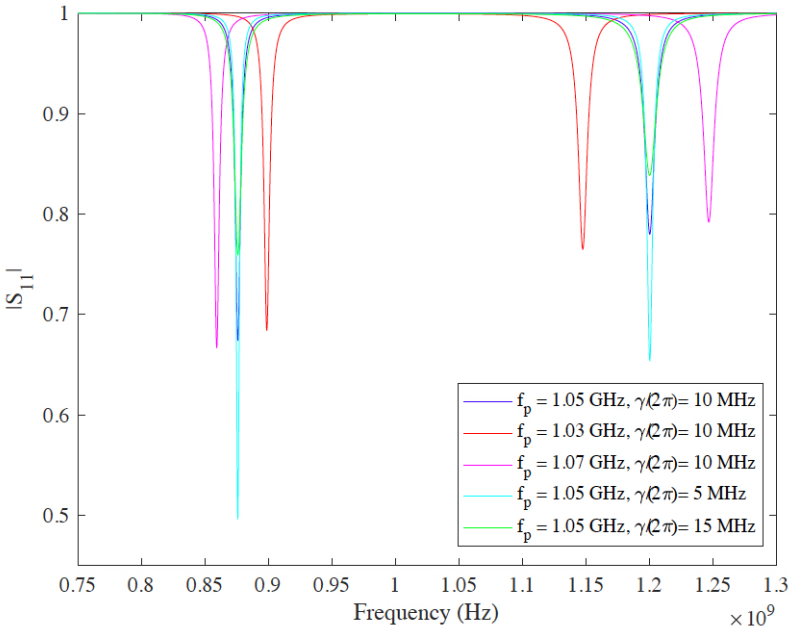

Figure 4.4: $|S_{11,f}|$ plotted as a function of frequency for various f_p and γ values.

resonance peaks became sharper and increased in magnitude. On the other hand, when γ was increased, the resonance peaks flattened.

4.5 Investigating the Effect of Negative μ'' on $|S_{11,f}|$

Finally, we can investigate what effect a negative imaginary component of the permeability, μ'', would have on the expected $|S_{11,f}|$ plot. From Eq. (4.2) we can deduce that if the magnetic plasma frequency, f_p, of the metamaterial is less than its resonant frequency, f_s, μ'' will be negative. We can plot the resulting permeability using Eqs. (4.1) and (4.2) and the following test parameters: $f_\mathrm{s} = 1$ GHz, $f_\mathrm{p} = 0.95$ GHz, and $\gamma/(2\pi) = 10$ MHz. The resulting plots are displayed in Fig. 4.5. As shown in Fig. 4.5, the imaginary component of the permeability, as shown in red, becomes negative at the resonance frequency. This is opposite to the effect seen in Fig. 4.1 when $f_\mathrm{p} > f_\mathrm{s}$. The real component of the permeability, as plotted in blue, crosses over zero and becomes negative at its magnetic plasma frequency, before spiking back up to a positive value at the resonant frequency. Thus, the negative portion of μ' occurs just below the resonant frequency instead of just above, as seen in Fig. 4.1. Using these values, and including test values of $f_0 = 1$ GHz, $Q_0 = 500$, $L_1 = 12$ nH, and $Z_0 = 50\ \Omega$, and $k = 0.065$, we can plot the expected $|S_{11,f}|$ curve produced from an LGR filled with a magnetic material with $f_\mathrm{s} > f_\mathrm{p}$, and thus negative μ''. To do this, we will again use Eqs. (4.1), (4.2), (4.10), and (4.11) to plot Eq. (4.12). The resulting plot of $|S_{11,f}|$ as a function of frequency is displayed in Fig. 4.6.

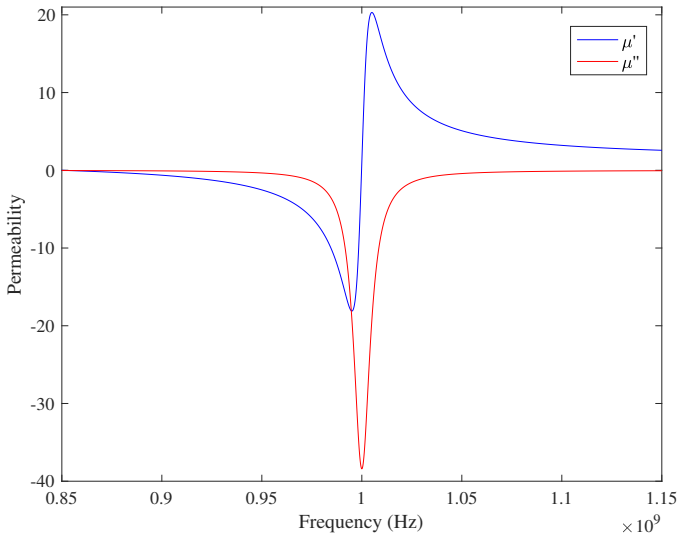

Figure 4.5: The real, μ', and imaginary, μ'', components of the SRR relative permeability plotted as a function of frequency when $f_{\mathrm{p}} = 0.95$ GHz, $f_{\mathrm{s}} = 1$ GHz, and $\gamma/(2\pi) = 10$ MHz.

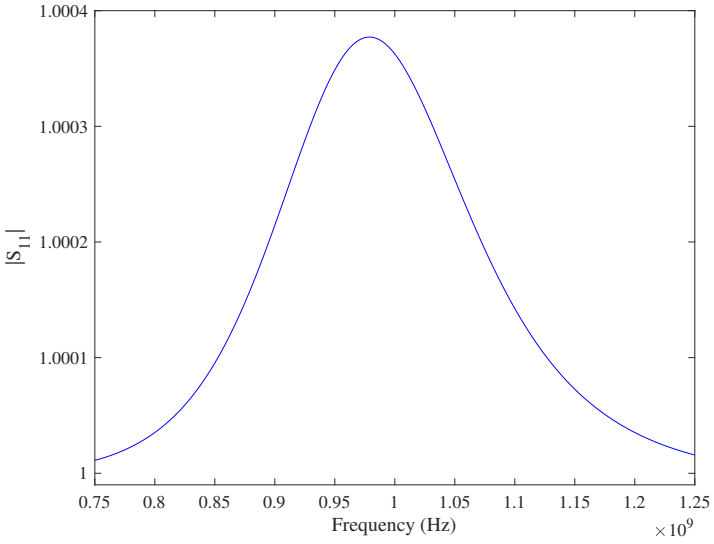

Figure 4.6: $|S_{11}|$ as a function of frequency when $f_{\mathrm{p}} = 0.95$ GHz, $f_{\mathrm{s}} = 1$ GHz, and $\gamma/(2\pi) = 10$ MHz.

As plotted in Fig. 4.6, the expected $|S_{11}|$ curve for an LGR filled with a magnetic material with a negative imaginary component of permeability is positive. This is an unphysical result as it suggests that the reflected voltage is greater than the voltage supplied to the LGR.

4.6 Experimentally Determining $|S_{11}|$ for an Array of SRRs

In this section, we will experimentally measure the $|S_{11}|$ signals over a range of microwave frequencies for SRR arrays using a LGR. We will load arrays of $N = 1$, 2, 3, and 4 SRRs into the one-loop-one-gap resonator. To begin, the coupling loop was oriented in order to acquire near-critical coupling. This position was found to be when the plane of the coupling loop was perpendicular to the bore axis. The coupling loop was then secured in this position using a set screw. Then, SRRs were placed as far as possible from the coupling loop as possible with their outermost slit opposite to the LGR's gap. As the array increased from one SRR, a 21 mm spacer was placed in between the SRRs. The LGR loaded with four SRRs is pictured in Fig. 4.7. Sweeps of the reflection coefficient

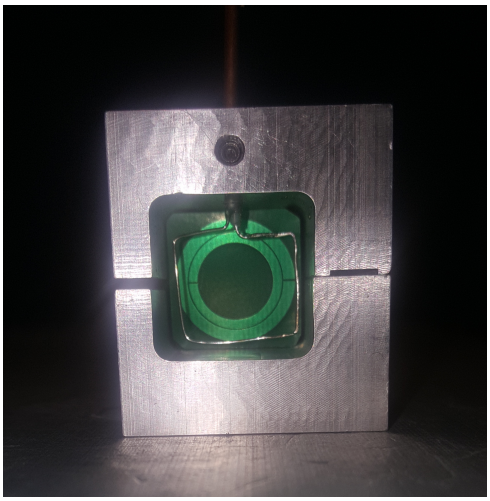

Figure 4.7: Array of four SRRs loaded into the one-loop-one-gap LGR spaced at approximately 21 mm apart.

over frequencies from 0.7 GHz to 1.3 GHz were taken for arrays of $N = 1$, 2, 3, and 4 SRRs. These signals were then converted to a linear scale using Eq. (2.1) and the resulting plots are shown in Fig. 4.8.

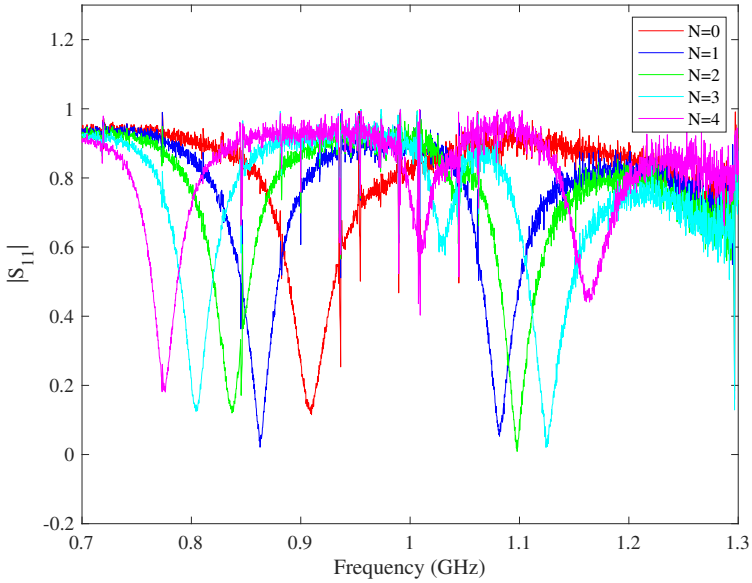

Figure 4.8: $|S_{11}|$ as a function of frequency for the one-loop-one-gap LGR when loaded with N SRRs spaced at approximately 21 mm apart.

Figure 4.8 shows $|S_{11}|$ plotted as a function of frequency for the five data sets collected. As expected, for an empty LGR a single resonance peak at about 0.9 GHz was measured. Then, when the bore of the LGR was filled with one SRR, a second resonance peak appeared at just below 1.1 GHz. As more SRRs were added, the peaks spread further apart. And, when three SRRs and four SRRs were loaded, a third dip appeared at a frequency of about 1 GHz. Finally, away from the resonances, $|S_{11}|$ was observed to decrease as frequency increased due to losses in the coaxial cable leading to the coupling loop. These observations are all consistent with what was shown in Fig. 3(a) of S. L. Madsen and J.S. Bobowski's paper for a similar experimental set-up [6].

Chapter 5

Permittivity of Cut Wire Arrays

5.1 Modelling Effective Permittivity

Just as SRR arrays have a negative permeability over a small range of microwave frequencies, cut wire arrays are known to display a negative permittivity at microwave frequencies. Using Maslovski *et al.*'s model describing the effective permittivity of an array of cut wires we were able to explore the permittivity of cut wire arrays of different dimensions [11]. To begin, we considered their model for ideally conducting wires, as denoted in Eq. (1.12). We considered an array of wires aligned with the z-axis with an electric field parallel to these wires. With these conditions, Eq. (1.12) reduced to,

$$\varepsilon_r = 1 - \frac{2\pi}{(ka)^2 \log(\frac{a^2}{4r_0(a-r_0)})}, \tag{5.1}$$

where ε_r is the relative effective permittivity, k is the wavenumber, a is the grid period, and r_0 is the wire radius. Note that $k = 2\pi/\lambda$ where λ denotes wavelength. Using this equation we were able to reproduce the solid lines plotted in Fig. 3 of Maslovski *et al.*'s paper. To do this, we set $r_0/a = 0.01$ and 0.1 in Eq. (5.1) and plotted ε_r as a function of ka for both ratios. The resulting plots are displayed in Fig. 5.1.

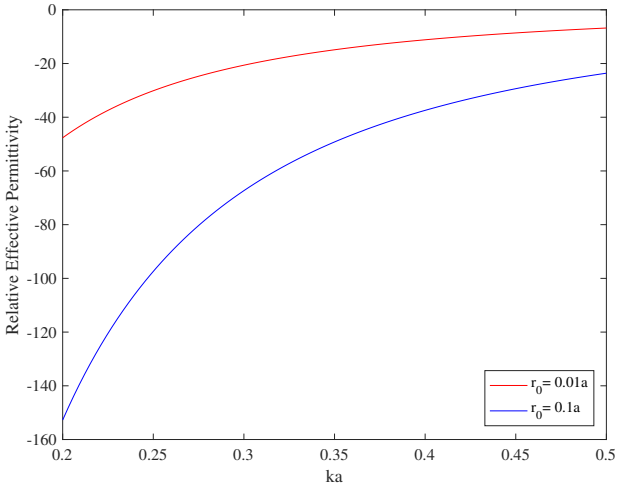

Figure 5.1: The effective permittivity of an array of ideally conducting wires as a function of ka. The plot produced when $r_0/a = 0.01$ is shown in red and the plot produced when $r_0/a = 0.1$ is shown in blue.

5.2 Designing Cut Wire Arrays

5.2.1 Modelling Possible Array Dimensions

Now, using this model, we designed a model for our cut wire array. Based on the SRRs and LGRs that we will be using, we have a predetermined grid period, a_0, of 21.6 mm. Using this value our goal is to determine suitable radii, r, for our cut wires to approximately satisfy the $r_0/a = 0.1$ ratio. This ratio was chosen as using this ratio we observed in Fig. 5.1 a larger effect on the permittivity. Using the selection of aluminum rod sizes from the McMaster Carr website, aluminum rods with diameters of 3/16-inches and 4.00 mm were chosen. This gives r_0 values of 2.38 mm and 2.00 mm, respectively. Next, in order to plot relative effective permittivity in terms of frequency by using of Eq. (5.1), wavenumber k was represented in terms of frequency using $k = 2\pi f/\mathrm{c}$. This gives the following,

$$\varepsilon_r = 1 - \frac{c^2}{2\pi(fa)^2 \log(\frac{a^2}{4r_0(a-r_0)})}, \tag{5.2}$$

where c is the speed of light in a vacuum. Eq. (5.2) was then plotted using r_0 values of 2.38 mm and 2.00 mm, shown in cyan and magenta respectively. The resonant frequencies of the SRRs and LGRs to be used alongside these cut wire arrays range from 0.6 to 1.2 GHz so the horizontal axis was set to plot this frequency range.

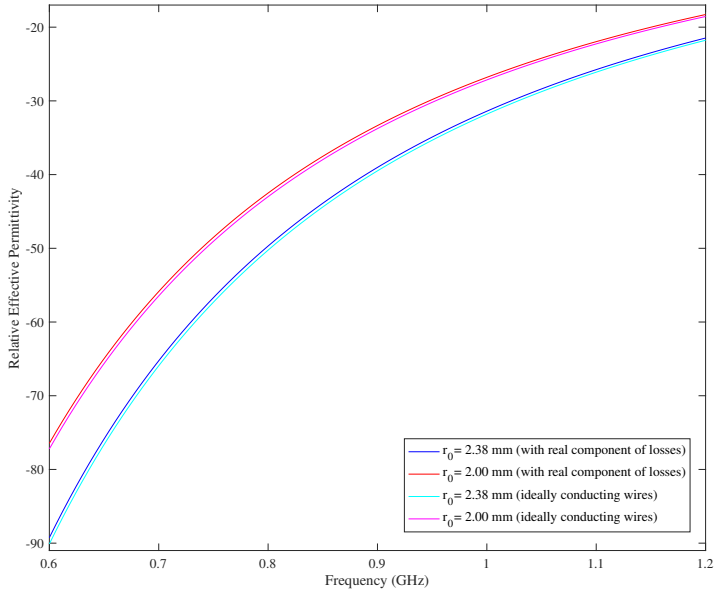

Figure 5.2: ε_r as a function of frequency. The plot produced for ideal conductors when $r_0 = 2.38$ mm is shown in cyan and when $r_0 = 2.00$ mm is shown in magenta. The real component of ε_r when losses are considered is plotted in blue (for $r_0 = 2.38$ mm) and red (for $r_0 = 2.00$ mm).

Equations (5.1) and (5.2) assume the cut wires used are ideally conducting and thus experience no losses. Maslovski *et al.* also proposed a correction to this model for lossy or loaded wires, which experience some surface impedance Z_s [20]. This impedance is given by Eq. (1.14) and the corrected permittivity is denoted by Eq. (1.15). Again, as we considered an array with wires aligned with the z-axis with an electric field parallel to these wires. Eq. (1.15) can be reduced to,

$$\varepsilon_r = 1 - \frac{2\pi}{(ka)^2 \log(\frac{a^2}{4r_0(a-r_0)}) - jka\frac{a}{r_0}\frac{Z_s}{\eta}}. \tag{5.3}$$

Substituting Eq. (1.14) into Eq. (5.3) we obtain a complex effective relative permittivity which can be expressed as $\varepsilon_r = \varepsilon' - j\varepsilon''$ where ε', the real component of permittivity, is given by,

$$\varepsilon' = \frac{(B+b)^2 + b^2 - 2\pi(B+b)}{(B+b)^2 + b^2}, \tag{5.4}$$

and ε'', the imaginary component of permittivity, is given by,

$$\varepsilon'' = \frac{2\pi b}{(B+b)^2 + b^2}. \tag{5.5}$$

For both Eqs. (5.4) and (5.5),

$$b \equiv \frac{ka^2}{r_0}\sqrt{\frac{\omega\varepsilon_0}{2\sigma}} \tag{5.6}$$

and,

$$B \equiv (ka)^2 \log\left(\frac{a^2}{4r_0(a-r_0)}\right). \tag{5.7}$$

The real part of the permittivity, as denoted in Eq. (5.4), was plotted as a function of frequency using r_0 values of 2.38 mm and 2.00 mm. The produced functions are plotted in blue and red on Fig. 5.2. This plot shows that when the real component of the conductor's losses is taken into account, the relative effective permittivity shifts very slightly upwards, towards the horizontal axis. However, the effect of losses is nearly negligible for good conductors.

The imaginary part of the permittivity was also plotted as a function of frequency using r_0 values of 2.38 mm and 2.00 mm. This plot is shown in Fig. 5.3. This figure shows that ε'' asymptotically approaches zero as frequency increases.

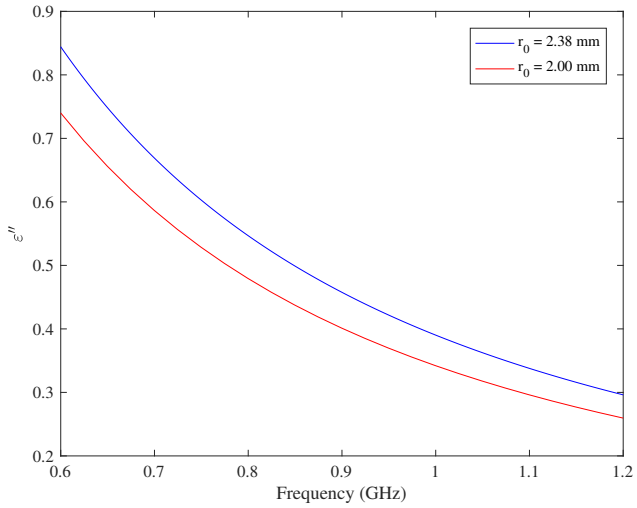

Figure 5.3: The imaginary component of ε_r, ε'', plotted as a function of frequency.

5.2.2 Modelling Permittivity of Our Array

Due to supply availability, our actual cut wire arrays were composed of aluminum wires of both 1/8-inch and 3/16-inch diameters. These result in radii of 1.59 mm and 2.38 mm. These are very similar and identical to 2.00 mm and 2.38 mm and, as such, are expected to yield similar results when Maslovski *et al.*'s models are plotted. To further explore our exact array dimensions, ε_r was plotted as a function of frequency using the ideally conducting wire model, denoted in Eq. (5.2). These plots are shown in Fig. 5.4. As predicted by Fig. 5.2, over the range of 0.6 GHz to 1.2 GHz, ε_r is modelled to be negative and increasing logarithmically as frequency increases.

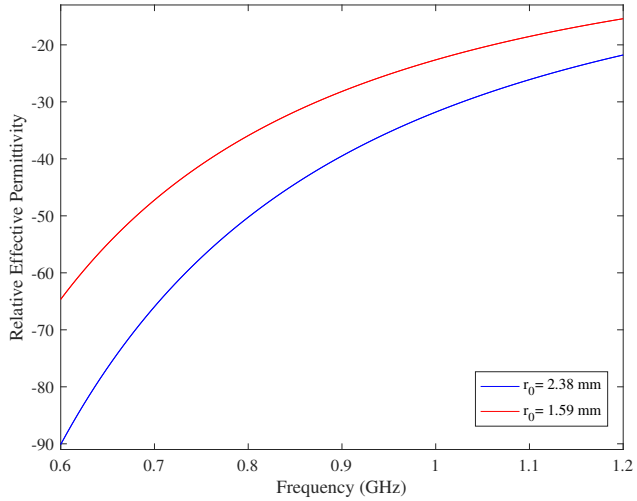

Figure 5.4: ε_r as a function of frequency modelled for ideal conductors.

5.3 Composing Cut Wire Arrays

5.3.1 One-Loop-One-Gap Resonator Arrays

Using aluminum wires of both 1/8-inch and 3/16-inch diameter, cut wire arrays were assembled. These arrays were then loaded into an LGR bore and their effect of the bores permeability was analyzed. In order to create secure arrays of cut wires with consistent dimensions, Teflon sheets were used. Teflon was used as it is expected to have no effect on the magnetic properties of the array. To begin, we created a $1 \times 1 \times N$ array of cut wires for measurements using the one-loop-one-gap resonator. This array consisted of four cut wires secured between two Teflon sheets with 1/8-inch thickness. The holders had approximate width and length of 16.4 mm and 85 mm, respectively. Similarly to the SRR arrays previously described, a grid period of $a \approx 21.6$ mm was used. This set-up is depicted in Fig. 5.5.

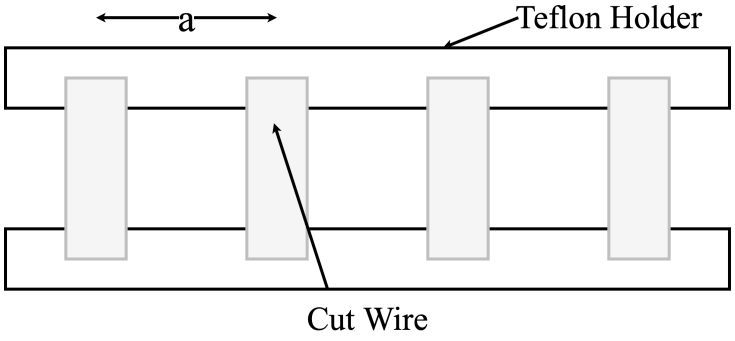

(a) Schematic model of cut wire array.

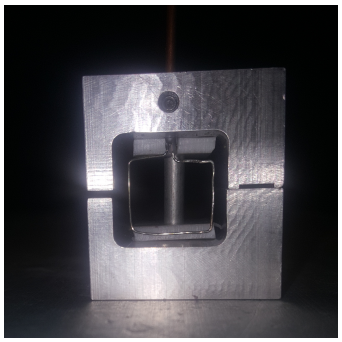

(b) $N = 4$ array loaded into one-loop-one-gap LGR.

Figure 5.5: $1 \times 1 \times N$ array of cut wires with grid period $a \approx 21.6$ mm

The counterbores in the a Teflon sheets had 1/16-inch depth and were created using both 1/8-inch and 3/16-inch diameter end mills for their respective arrays. The cut wires were cut to by a height of approximately 18.5 mm so as to fit tightly into the LGR bore while in their holders. Additionally, Teflon rods of both 1/8-inch and 3/16-inch diameter and a height of approximately 18.5 mm were also made. These were used to replicate the geometry of our cut wire set-up while taking measurements with no cut wires. This enabled us to accurately determine the effect of the addition of aluminum wires. These Teflon rods were used as place holders for arrays of $N = 1$, 2, and 3.

5.3.2 Two-Loop-One-Gap Resonator Arrays

Similar cut wire arrays were constructed to be used for measurements with the two-loop-one-gap resonator. However, this time $2 \times 2 \times N$ arrays were made. Thus, $N = 1$, 2, 3 and 4 correspond to four, eight, twelve, and sixteen cut wires, respectively. The wires used had

the same dimensions as for the $2 \times 2 \times N$ arrays. A side-view of the array is shown in Fig. 5.6(a) and the array loaded into the two-loop-one-gap LGR is depicted in Fig. 5.6(b).

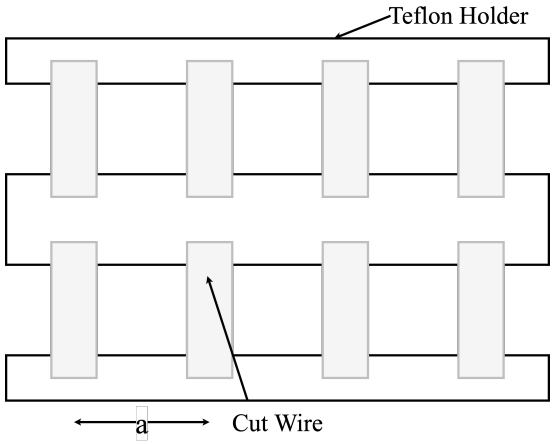

(a) Schematic model of cut wire array.

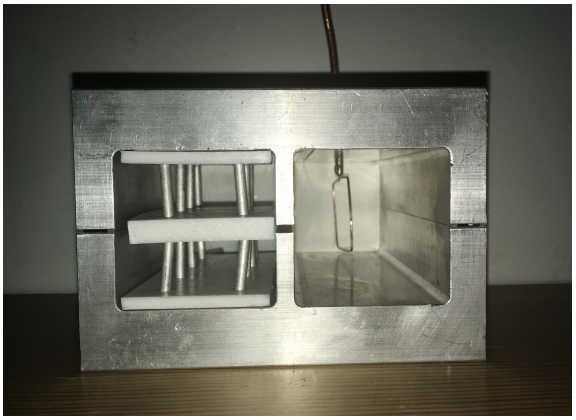

(b) $N = 4$ array loaded into two-loop-one-gap LGR.

Figure 5.6: $2 \times 2 \times N$ array of cut wires with grid period $a \approx 21.6$ mm

It is important to note that there are sixteen cut wires in total. Moreover, the bottom at top Teflon sheets have 1/8-inch thickness and the middle sheet has 1/4-inch thickness and the grid period of the cut wire array is $a \approx 21.6$ mm. The holders had approximate width and length of 39 mm and 85 mm, respectively.

5.4 Measuring $|S_{11}|$ of Cut Wire Arrays

5.4.1 One-loop-one-gap Loop Gap Resonator (LGR)

3/16-inch Diameter Aluminum Rods

In order to explore the permeability of cut wire arrays, we measured the reflection coefficient of the signal, $|S_{11}|$, for arrays of different numbers of cut wires. Again, the coupling loop of the one-loop-one-gap resonator was oriented perpendicular to the bore axis in order to acquire near-critical coupling and secured. We began by measuring the reflection coefficient, $|S_{11}|$, of the empty LGR. We then repeated this measurement for arrays of four ($N = 4$), three ($N = 3$), two ($N = 2$), one ($N = 1$), and zero ($N = 0$) aluminum cut wires of 3/16-inch diameter. The LGR loaded with four aluminum cut wires is displayed in Fig. 5.5(b). As an aluminum cut wire was removed, a Teflon rod of the same dimensions filled its place between the two Teflon sheets. For consistency, these Teflon rods were placed closest to the coupling loop to keep the aluminum cut wires as far as possible from the coupling loop. Thus, the $N = 0$ case describes a situation in which four Teflon rods were placed between the Teflon sheets. The resulting $|S_{11}|$ curves were converted to a linear scale using Eq. (2.1) and plotted as shown in Fig. 5.7(a).

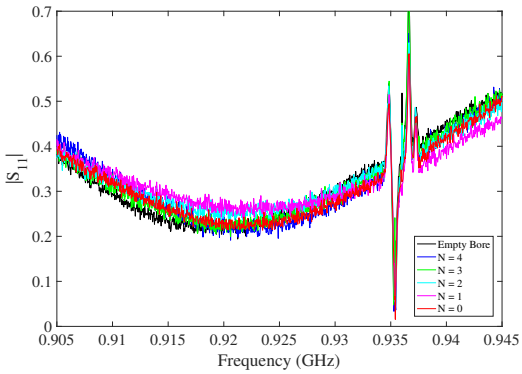

(a) All Arrays

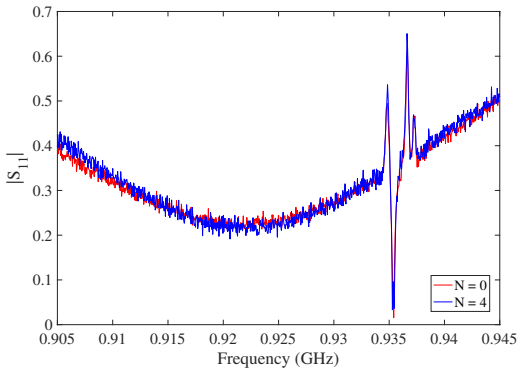

(b) Only $N = 0$ and $N = 4$

Figure 5.7: $|S_{11}|$ as a function of frequency measured for an empty bore and for a 1-D array of N 3/16-inch diameter aluminum rods.

From Fig. 5.7(a) we can qualitatively conclude that the addition of cut wires to the bore of the resonator has a very minimal and non-systematic effect on the measured $|S_{11}|$ curves. Each resonance occurs at a frequency of approximately 0.92 GHz and the dips have similar width and depth. This effect is further exemplified in Fig. 5.7(b) in which only arrays of $N = 0$ and $N = 4$ are overlayed. This $|S_{11}|$ curves are nearly identical despite the large difference in array composition. This was not the result we expected. As we add aluminum cut wires to the bore, the open volume of the bore will decrease. Thus, as the inductance of the LGR is proportional to the volume, we expected the inductance of the LGR to decrease as arrays of cut wires are loaded into the resonator's bore. This, in turn, would be expected to increase the resonance frequency denoted by Eq. (1.21). However, for the one-loop-one-gap resonator, we observed no systematic changes as the bore of the LGR is filled with cut wires.

1/8-inch Diameter Aluminum Rods

These measurements were replicated with arrays N 1/8-inch aluminum cut wires. The resulting reflection coefficients, $|S_{11}|$, were plotted as a function of frequency and are displayed in Fig. 5.8. Again, the addition of the aluminum cut wires had nearly no effect on the produced $|S_{11}|$ curves.

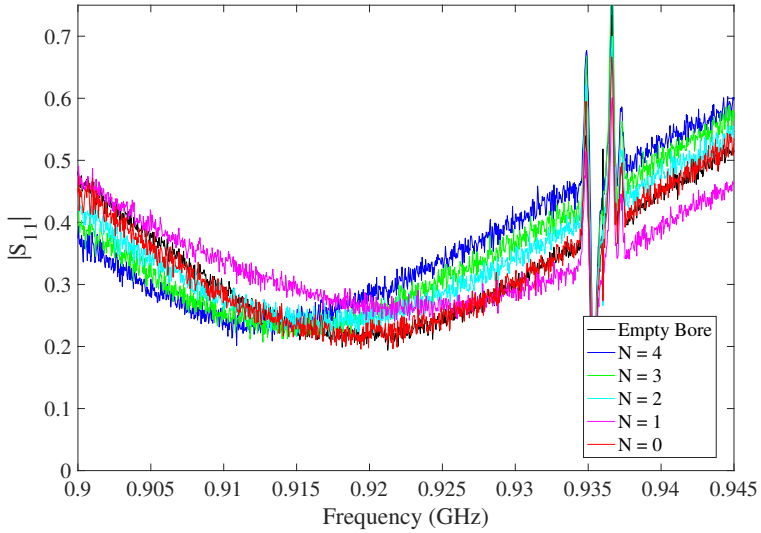

Figure 5.8: $|S_{11}|$ as a function of frequency measured for an empty bore and for a 1-D array of N 1/8-inch diameter aluminum rods.

5.4.2 Two-loop-one-gap Loop Gap Resonator (LGR)

3/16-inch Diameter Aluminum Rods

This experimental procedure was then replicated using the two-loop-one-gap resonator. Again, to begin, we oriented the coupling loop in order to critically couple the LGR with the coupling loop. Once this orientation, in which the plane of the coupling loop was nearly parallel with the bore's axis, was found, the coupling loop was secured with a set screw and arrays of 3/16-inch diameter aluminum rods were loaded into the bore of the LGR. This time, however, we were working with $2 \times 2 \times N$ arrays of cut wires. The array set-up displayed in Fig. 5.6 was used. This array was centered in the bore of the resonator not containing the coupling loop. This experimental set-up is depicted for an $N = 4$ array of cut wires in Fig. 5.6(b). Similarly to in the one-loop-one-gap case, when the number of aluminum rods was reduced, they were removed from the side closest to the coupling loop first and replaced with Teflon rods. The resulting linearized plots of $|S_{11}|$ as a function of frequency for an empty resonator and for when the bore was filled with various arrays of aluminum wires of 3/16-inch diameter are displayed in Fig. 5.9.

Unlike with the one-loop-one-gap resonator, these measurements show that the resonance frequency decreases as N increases. This does not agree with what is expected from Eq. (1.21). To further explore how the resonance peaks change with arrays of cut wires, we plotted $|S_{11}|$ as a function of $(f/f_0) - 1$ as shown in Fig. 5.10 . While the plots vary slightly in depth and width, there are no observed systematic changes as N changes.

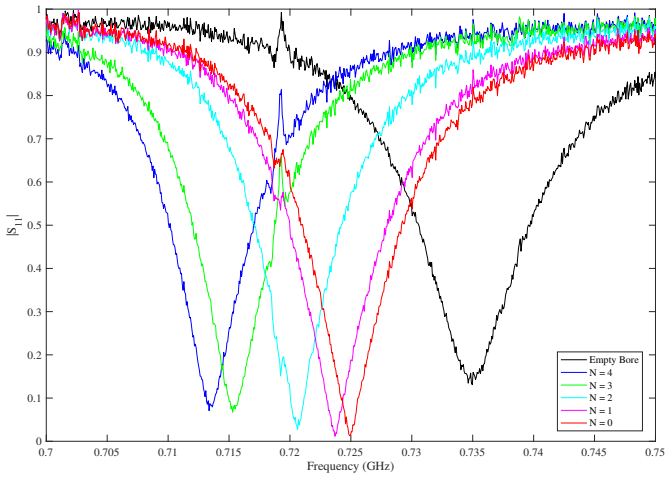

Figure 5.9: $|S_{11}|$ as a function of frequency for $2 \times 2 \times N$ arrays of N 3/16-inch diameter aluminum rods.

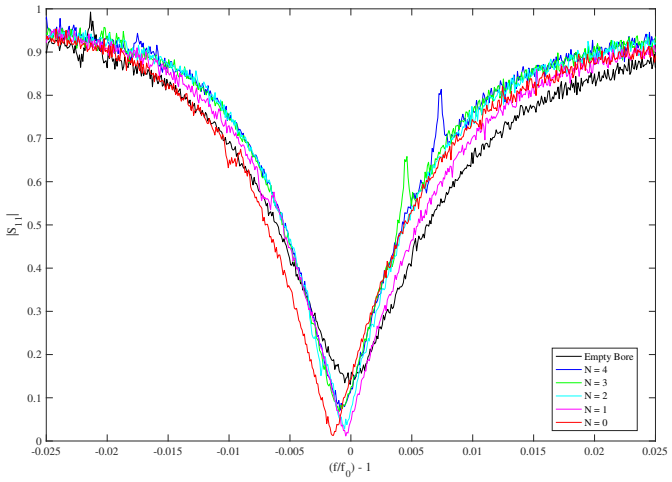

Figure 5.10: $|S_{11}|$ as a function as a function of $(f/f_0) - 1$ for $2 \times 2 \times N$ arrays of N 3/16-inch diameter aluminum rods.

1/8-inch Diameter Aluminum Rods

Lastly, this procedure was reproduced using 1/8-inch diameter aluminum cut wires. Similarly to what we observed with the 3/16-inch diameter rods, the resonance frequency decreases as N increases. This result is displayed in Fig. 5.11. When the reflection coefficient of the signal, $|S_{11}|$, is plotted as a function of $(f/f_0) - 1$, as shown in Fig. 5.12, no systematic changes are observed as N is varied.

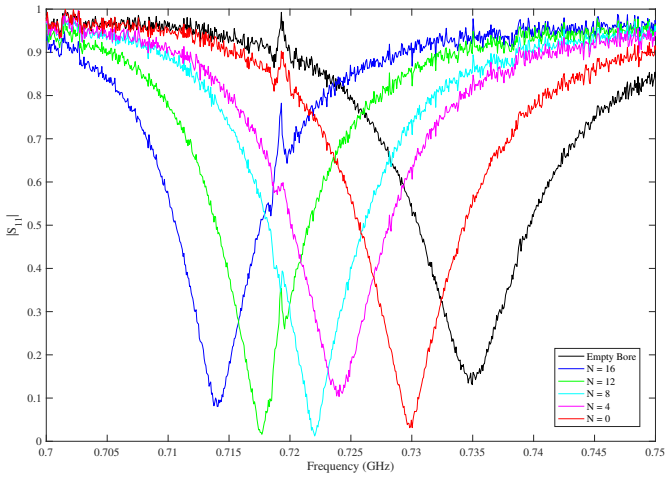

Figure 5.11: $|S_{11}|$ as a function of frequency for $2 \times 2 \times N$ arrays of N 1/8-inch diameter aluminum rods.

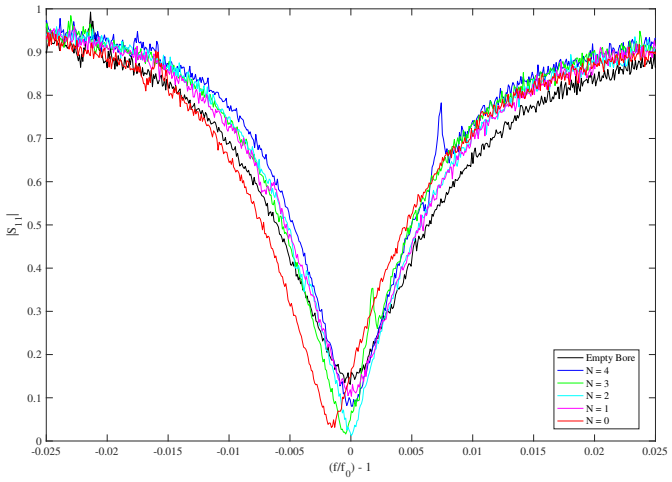

Figure 5.12: $|S_{11}|$ as a function as a function of $(f/f_0) - 1$ for $2 \times 2 \times N$ arrays of N 1/8-inch diameter aluminum rods.

Overall, as we add cut wires to the bore of the LGR, we qualitatively observed very minimal changes in the produced $|S_{11}|$ reflections. No additional resonance peaks are observed and the width and depth of the LGR's resonance is nearly independent of cut wire array size. This suggests that, as $|S_{11}|$ depends on permeability of the material inside of the LGR's bore, the addition of cut wires has a very minimal effect on the bore's permeability.

Chapter 6

Modelling the Effective Impedance of a Partially Filled LGR

In Chapter 4.2, we found the effective impedance of the LGR with a completely filled bore, Z_{f}, and represented it in terms of its real, Eq. (4.10), and imaginary, Eq. (4.11), components as $Z_{\mathrm{f}} = R_{\mathrm{f}} + jX_{\mathrm{f}}$. Now, we will explore how this effective impedance varies when the resonator bore is only partially filled with the magnetic material. First, we will find the inductance of the empty-bore resonator. To do this, we must define our resonator length as s and its cross-sectional area as A. Then, using the formula for inductance of a solenoid, $L = \frac{\mu_0 N^2 A}{s}$, substituting the number of turns, $N = 1$, we obtain the inductance of the empty-bore resonator:

$$L_0 = \frac{\mu_0 A}{s}. \tag{6.1}$$

We will now suppose the LGR has been partially filled with the magnetic material with relative permeability $\mu_{\mathrm{r}} = \mu' - j\mu''$. This material has length $x < s$ and a filling factor, η, which is defined as $\eta = x/s$. In order to find the inductance of the empty portion of this LGR, L_{e}, we must redefine the length as $s - x$. This gives us the inductance of the empty portion of the bore to be

$$L_{\mathrm{e}} = \frac{\mu_0 A}{s - x}. \tag{6.2}$$

To simplify this equation, we can factor out an s in the denominator and then substitute in Eq. (6.1) to obtain

$$L_{\mathrm{e}} = \frac{L_0}{1 - \eta}. \tag{6.3}$$

We can do a similar analysis for the inductance of the filled portion of the bore. However, this time we must change the length to x as well as include the relative permeability of the magnetic material filling the bore. This gives us the inductance of the filled portion of the bore,

$$L_{\mathrm{f}} = \frac{\mu_0 \mu_{\mathrm{r}} A}{x}. \tag{6.4}$$

Similarly, in order to put this equation in terms of L_0 we can substitute in $x = \eta s$ and then define $\mu_0 A/s$ as L_0 using Eq. (6.1). This gives us the desired result for the impedance of the filled portion of the bore,

$$L_{\mathrm{f}} = \frac{\mu_{\mathrm{r}} L_0}{\eta}. \tag{6.5}$$

Now, we will argue that the effective inductance, L, of the partially-filled LGR can be determined by the parallel combination of L_{e} and L_0. We can imagine that if there was a current applied through a coupling loop on one side of the bore, a magnetic field, $\vec{B}$, would permeate the entire bore of the LGR. Thus, the magnetic flux, Φ would be equal through all cross-sections of the LGR – independent of whether there was magnetic material filling that area. This means that the induced emf, ε, is equal for the region containing the magnetic material and for the empty region as $\varepsilon = -d\Phi/dt$ and the magnetic flux through the entire resonator bore is unchanged. Thus, as the induced emf is the same through each region, we can combine L_{e} and L_0 as though they were in parallel in a simple circuit. This set-up is analogous as the voltage change over two inductors in parallel is equal, similarly to the induced emf through each region of the LGR. Using this model we obtain,

$$\frac{1}{L} = \frac{1}{L_{\mathrm{e}}} + \frac{1}{L_{\mathrm{f}}}. \tag{6.6}$$

From here, we can obtain a common denominator, take the reciprocal of each side, and substitute in Eqs. (6.3) and (6.5) to obtain

$$L = \frac{\mu_{\mathrm{r}} L_0^2}{\eta(1-\eta)} \times \frac{\eta(1-\eta)}{L_0\eta + \mu_{\mathrm{r}} L_0(1-\eta)}. \tag{6.7}$$

We can now cancel terms and substitute in $\mu_{\mathrm{r}} = \mu' - j\mu''$. This gives us,

$$L = L_0 \frac{(\mu' - j\mu'')}{(\mu' - j\mu'') - \eta(\mu' - j\mu'') + \eta}. \tag{6.8}$$

Next, we can collect like terms and multiply by the complex conjugate of the denominator in order to remove imaginary terms from the denominator. This yields,

$$L = L_0 \frac{(\mu' - j\mu'')}{(\mu'(1-\eta)+\eta) - j\mu''(1-\eta)} \times \frac{(\mu'(1-\eta)+\eta) + j\mu''(1-\eta)}{(\mu'(1-\eta)+\eta) + j\mu''(1-\eta)}. \tag{6.9}$$

From here, the denominator and numerator are multiplied out and the imaginary and real components from the numerator are separated in order to write the effective inductance of the partially filled LGR as:

$$L = L_0 \left(\frac{|\mu_{\mathrm{r}}|^2(1-\eta) + \mu'\eta}{[\eta + \mu'(1-\eta)]^2 + [\mu''(1-\eta)]^2} - j \frac{\mu''\eta}{[\eta + \mu'(1-\eta)]^2 + [\mu''(1-\eta)]^2} \right), \tag{6.10}$$

where $|\mu_{\mathrm{r}}|^2 = (\mu')^2 + (\mu'')^2$. Equation (6.10) can be expressed as $L = \ell L_0$ where $\ell = \ell'$ - $j\ell''$. Here, the real component of ℓ, ℓ', is denoted,

$$\ell' = \frac{|\mu_{\mathrm{r}}|^2(1-\eta) + \mu'\eta}{[\eta + \mu'(1-\eta)]^2 + [\mu''(1-\eta)]^2}, \tag{6.11}$$

and its imaginary component, ℓ'' is denoted,

$$\ell'' = \frac{\mu''\eta}{[\eta + \mu'(1-\eta)]^2 + [\mu''(1-\eta)]^2}. \tag{6.12}$$

Before moving on, we will show that the results we obtained for the effective inductance of the partially filled LGR bore, L, make sense for when $\eta = 0$, $\eta = 1$, and $\mu_r = 1$. First, when $\eta = 0$ we obtain $L = L_0$. This makes sense as if the filling factor is zero, the LGR is empty and thus should have the inductance given for an empty bore. Next, when $\eta = 1$ we obtain $L = L_0(\mu' - j\mu'')$. This denotes the inductance of the LGR when its bore is completely filled with a magnetic material of relative permeability $\mu_r = \mu' - j\mu''$. Again, this makes sense, as when the filling factor is one, the LGR bore is completely filled thus has the inductance expected for an LGR with a filled bore. Lastly, when $\mu_r = 1$, $L = L_0$. This makes sense as $\mu_r = \frac{\mu}{\mu_0}$. So, if $\mu_r = 1$, the permeability of the magnetic material, μ is equal to the permeability of free space, μ_0. Thus, it follows that the inductance would be equal to the inductance of an LGR with an empty bore.

Now, we can modify Eqs. (4.10) and (4.11) so they represent the effective impedance of an LGR with a partially filled bore. Previously, as the bore was completely filled with the magnetic material, its inductance was given by $L = (\mu' - j\mu'')L_0$. Now, we have determine the partially filled bore's inductance is given as $L = (\ell' - j\ell'')L_0$ where ℓ' is denoted in Eq. (6.11) and ℓ'' is given by Eq. (6.12). This is the only change we made to this model to represent a partially filled bore. Thus, Eqs. (4.10) and (4.11) can easily be modified to represent an LGR with its bore partially filled with a magnetic material by substituting μ' with ℓ' and μ'' with ℓ''. This results in the effective impedance of the partially filled bore, Z, to be given by $Z = R + jX$, where the real component of the effective impedance is,

$$R = \frac{\omega L_1(\omega/\omega_0)k^2[\frac{\ell'}{Q_0}\sqrt{\omega/\omega_0} + \ell''(\omega_0/\omega)]}{[\frac{1}{Q_0}\sqrt{\omega/\omega_0} + \ell''(\omega/\omega_0)]^2 + [\ell'(\omega/\omega_0) - (\omega_0/\omega)]^2}, \tag{6.13}$$

and the imaginary component is,

$$X = \omega L_1 \left(1 - \frac{(\omega/\omega_0)k^2[\ell''[\frac{1}{Q_0}\sqrt{\omega/\omega_0} + \ell''(\omega/\omega_0)] + \ell'[\ell'(\omega/\omega_0) - (\omega_0/\omega)]]}{[\frac{1}{Q_0}\sqrt{\omega/\omega_0} + \ell''(\omega/\omega_0)]^2 + [\ell'(\omega/\omega_0) - (\omega_0/\omega)]^2}\right). \tag{6.14}$$

Chapter 7

Permeability of NIM Arrays

7.1 Composing NIM Arrays

In this section, we will explore the permeability of arrays of both SRRs and aluminum cut wires. In order to do this, the array configurations in Figs. 5.5 and 5.6 were modified to include SRRs. The $1 \times 1 \times N$ array composition is shown on the left of Fig. 7.1 and an SRR is shown on the right. Again, Teflon sheets of 1/8-inch thickness were used to secure

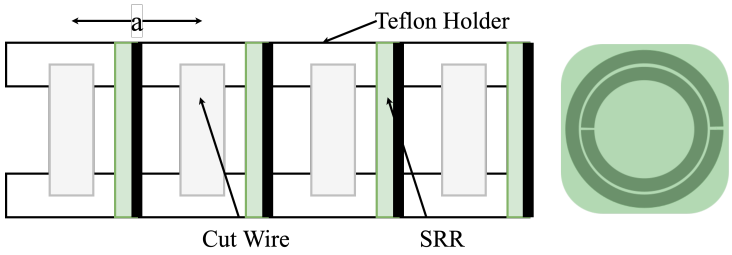

Figure 7.1: $1 \times 1 \times N$ array of SRRs and cut wires with grid period $a \approx 21.6$ mm beside single SRR.

the wires in the array. To ensure a distance of $a/2$ between the center of the cut wire and the SRR, the cut wire indents could not be centred on the Teflon holders. We had to account for the fact that the SRR was attached to a substrate with a total thickness of 1.54 mm. Thus, to create this consistent $a/2$ distance, the Teflon holders had length of approximately 10.4 mm from one edge to the centre of the cut wire indent, and 8.2 mm from here to the opposite edge. They had an approximate width of 16.5 mm. In Fig. 7.1, the black side depicts where the SRR is secured on its green substrate.

A similar modification, which is shown in Fig. 7.2, was used to modify the $2 \times 2 \times N$ arrays of cut wires to also incorporate SRRs. Comparably to the arrays of solely cut wires, the top Teflon sheets used to secure the array in place had 1/8-inch thickness while the centre sheet had 1/4-inch thickness. The 1/16-inch counterbores used to hold the cut wires were also slightly off-centred as for the one dimensional arrays to ensure a consistent distance of $a/2$ between the cut wires and the SRRs. However, the width of these Teflon sheets was approximately 39 mm. The arrays displayed in Fig. 7.1 and 7.2 are shown loaded into the bores of their respective LGR in Fig. 7.3(a) and (b), respectively.

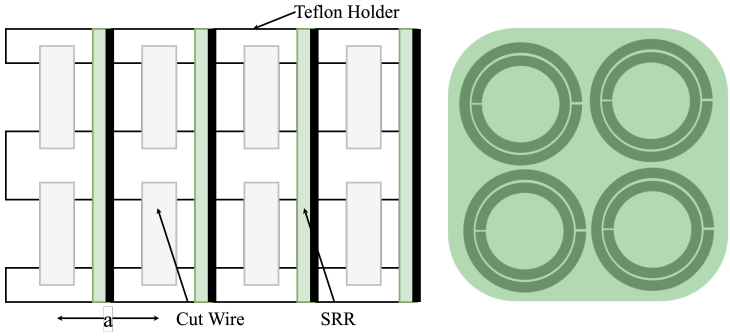

Figure 7.2: $2 \times 2 \times N$ array of SRRs and cut wires with grid period $a \approx 21.6$ mm beside 2×2 plane of SRRs.

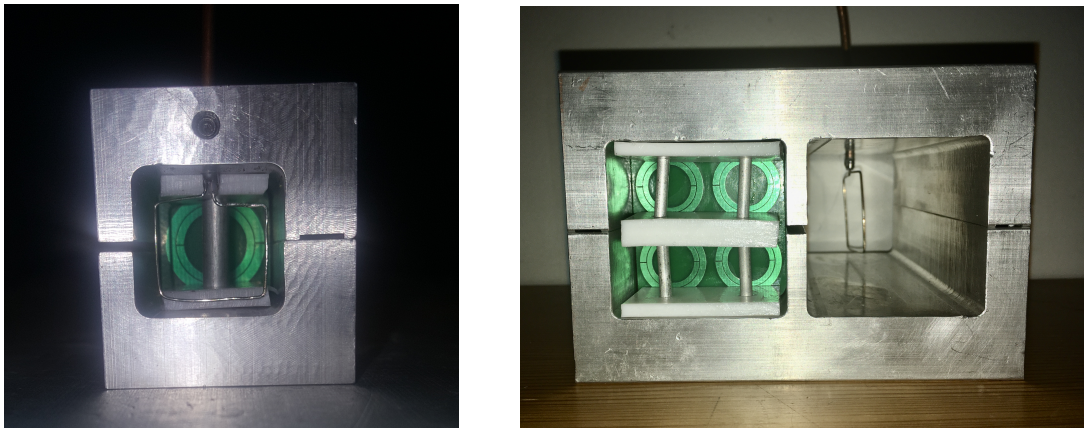

(a) $1 \times 1 \times N$ array in one-loop-one-gap LGR

(b) $2 \times 2 \times N$ array in two-loop-one-gap LGR

Figure 7.3: Experimental set-up fpr $N = 4$ arrays of SRRs and aluminum cut wires loaded into LGRs.

7.2 Measuring $|S_{11}|$ of NIM Arrays

7.2.1 One-loop-one-gap

To begin, we explored the $1 \times 1 \times N$ array using the one-loop-one-gap LGR. As previously described, the coupling loop was set perpendicular to the bore axis to acquire near-critical coupling and secured. Then, a single SRR and a single Teflon rod (3/16-inch diameter) were loaded into the bore as far from the coupling loop as possible. In addition, the SRR was loaded in first followed by the Teflon rod to reduce the end effects on the SRR, which can occur as the induced magnetic field loops around the edges and into the bore of the LGR. This process was repeated using a single SRR and a single aluminum rod (3/16-inch diameter) and subsequently carried out for arrays of $N = 2$, 3, and 4 SRRs and both aluminum and Teflon rods of both 1/8-inch and 3/16-inch diameter. The loaded LGR used for these measurements is pictured in Fig. 7.3(a). The plots of $|S_{11}|$ as a

function of frequency, shown in Appendix A, show little variation when aluminum rods are used instead of Teflon rods. The only minimal change observed was, as the volume of aluminum of the bore increased, the resonance peaks shifted slightly closer together. Moreover, the resonance curves show similar qualitative features to those displayed in Fig. 4.8, in which the reflection coefficient SRR arrays was measured. The most significant shift was observed between the $N = 4$ arrays of 3/16-inch diameter wires, as shown in Fig. 7.4. However, the variation in $|S_{11}|$ curve is still very minimal. This suggests that the aluminum rods have an insignificant effect on the permeability of the NIM.

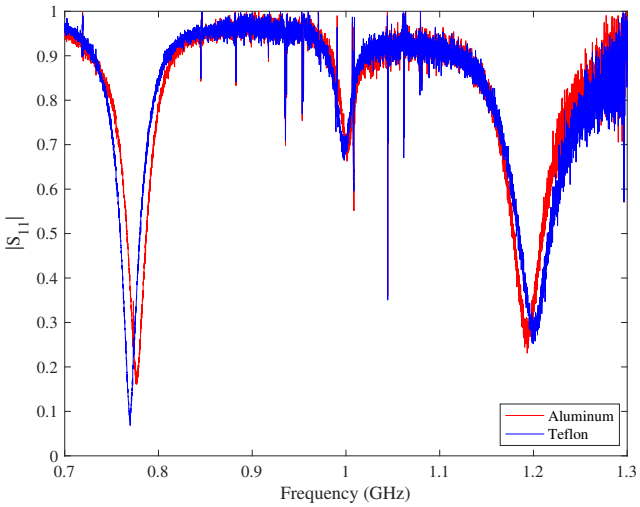

Figure 7.4: $|S_{11}|$ as a function of frequency when four SRRs and four 3/16-inch diameter aluminum cut wires (shown in red) or four 3/16-inch diameter Teflon rods (shown in blue) are loaded in the bore of the LGR.

7.2.2 Two-loop-one-gap

Similar measurements were taken using the $2 \times 2 \times N$ NIM array using the two-loop-one gap LGR using the experimental set-up depicted in Fig. 7.3(b). Again, we loaded in the NIM in the bore opposite the coupling loop and did not place the SRRs at the edge of the bore to reduce end effects. The obtained $|S_{11}|$ curves are displayed in Appendix B. Once again, the addition of cut wires had a very minimal effect on the produced resonance peaks. The only minimal change observed was when aluminum cut wires were added to the array, the resonant frequencies of $|S_{11}|$ were slightly lower. This effect becomes slightly more prominent as the volume of aluminum loaded into the bore of the LGR increases and is most pronounced when comparing the $N = 4$ arrays of 3/16-inch diameter wires, as shown in Fig. 7.5.

This result is consistent with what we observed when we filled the bore of the two-loop-one-gap resonator with only aluminum cut wires (no SRRs) and compared the results to

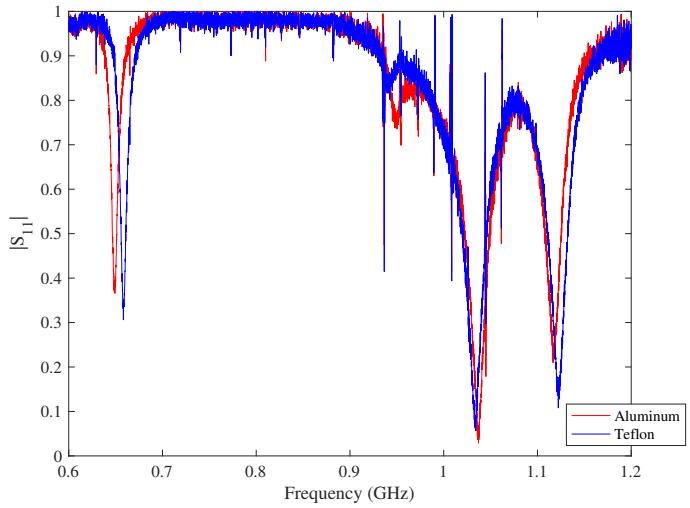

Figure 7.5: $|S_{11}|$ as a function of frequency when sixteen SRRs and sixteen 3/16-inch diameter aluminum cut wires (shown in red) or sixteen 3/16-inch diameter Teflon rods (shown in blue) are loaded in the bore of the LGR.

when the bore was filled with Teflon rods. For these measurements, we observed that as the volume of aluminum in the bore increased, the resonance frequency of the single resonance dip decreased. However, despite the small decrease in resonance frequency observed as the volume of aluminum in the bore increases, the shape and depth of the resonance curves do not change with the addition of the aluminum rods. So, in conclusion, similarly to for the $1 \times 1 \times N$ NIM arrays, the addition of cut wires has little to no effect on the produced resonance curves and thus an insignificant effect on the permeability of the NIM.

7.3 Determining the Permeability of NIM Arrays

In order to determine the permeability of the 1-D array of SRRs and cut wires, we can fit the $|S_{11}|$ curves using Pendry *et al.*'s model [1] which we stated in Eqs. (4.1) and (4.2). However, this model must be modified to fit data with three resonance peaks. Thus, Eqs. (4.1) and (4.2) will be extended to Eqs. (7.1) and (7.2), respectively. It has been shown that an NIM with an $|S_{11}|$ curve with three defined resonant dips will observe a permeability with two resonances [6].

$$\mu' = 1 - \frac{[1-(f_{s,1}/f_{p,1})^2][1-(f_{s,1}/f)^2]}{[1-(f_{s,1}/f)^2]^2+[\gamma_1/(2\pi f)]^2} - \frac{[1-(f_{s,2}/f_{p,2})^2][1-(f_{s,2}/f)^2]}{[1-(f_{s,2}/f)^2]^2+[\gamma_2/(2\pi f)]^2} \tag{7.1}$$

$$\mu'' = \frac{[\gamma_1/(2\pi f)][1-(f_{s,1}/f_{p,1})^2]}{[1-(f_{s,1}/f)^2]^2+[\gamma_1/(2\pi f)]^2} + \frac{[\gamma_2/(2\pi f)][1-(f_{s,2}/f_{p,2})^2]}{[1-(f_{s,2}/f)^2]^2+[\gamma_2/(2\pi f)]^2} \tag{7.2}$$

By combining these equations with the model we have for the effective impedance of LGR partially filled with magnetic material, as denoted in Eqs. (6.11) to (6.14), we are able to fit the data we have collected for a partially filled resonator using the MATLAB code shown in Appendix C. From this fit we will extract parameters for resonant frequency, f_s, magnetic plasma frequency, f_p, and $\gamma_s/(2\pi)$, for both resonances expected for the NIM permeability. Using the fit values found in Table 2 in "The Complex Permeability of Split-Ring Resonator Arrays Measured at Microwave Frequencies" by S.L. Madsen and J.S. Bobowski [6], we set the following initial parameters: $f_{p,1} = 0.930$ GHz, $f_{s,1} = 0.850$ GHz, $\gamma = \gamma_{s,1}\sqrt{f/f_{s,1}}$, $\gamma_{s,1}/(2\pi) = 33$ MHz, $f_{p,2} = 1.031$ GHz, $f_{s,2} = 1.015$ GHz, $\gamma = \gamma_{s,2}\sqrt{f/f_{s,2}}$, and $\gamma_{s,2}/(2\pi) = 11$ MHz. These parameters provide only a starting point for the fit and will be modified for our data set. Additionally, $k = 0.3k_{sc}$ where k_{sc} is initially set to 1 but will be specified to each data set as it depends on the specific coupling loop orientation. Additionally, L_1=42.54 nH $L_{1,sc}$ where $L_{1,sc}$ is initially set to 1.75. In our first fit, we will determine k_{sc} and $L_{1,sc}$ which will then be used for all subsequent fits. Now, we can plot $|S_{11}|$ as a function of frequency for the data we have collected and fit it to $|S_{11}|$ as determined by the following model,

$$|S_{11}| = \frac{\sqrt{[(|Z|^2/Z_0^2) - 1]^2 + [2(X/Z_0)]^2}}{[(|Z|^2/Z_0^2) + 1] + 2(R/Z_0)}, \tag{7.3}$$

where $|Z|^2 = R^2 + X^2$ and R and X are given by Eqs. (6.13) and (6.14), respectively. The following values are assumed $Z_0 = 50\Omega$, $f_0 = 857.7$ MHz, and $Q_0 = 49.08$. The first data set we will fit was collected while an $N = 4$ array of SRRs and 3/16-inch Teflon rods was loaded into the LGR bore. This data set and fit is shown in Fig. 7.6(a).

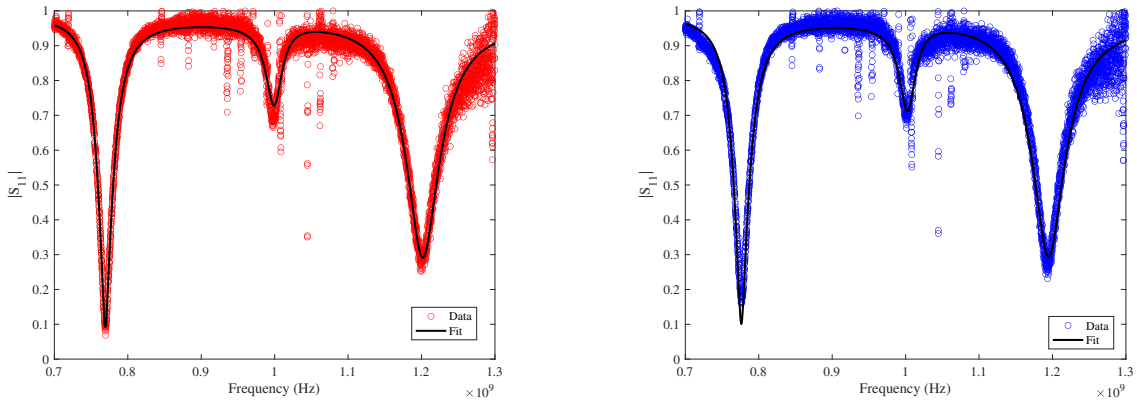

(a) Teflon (b) Aluminum

Figure 7.6: $|S_{11}|$ as a function of frequency measured for one-loop-one-gap resonator filled with four SRRs and four 3/16-inch diameter rods and fit using Pendry *et al.*'s model modified for a partially filled LGR.

From here, we determined and set k_{sc} to 1.54 and $L_{1,sc}$ to 1.1339. The obtained parameters for $f_{p,1}$, $f_{s,1}$, $\gamma_{s,1}/(2\pi)$, $f_{p,2}$, $f_{s,2}$, and $\gamma_{s,2}/(2\pi)$ are presented in Table 7.1. The same fit was

Table 7.1: Best fit parameters for one-loop-one-gap resonator filled with four SRRs and four 3/16-inch diameter Teflon rods.

$f_{s,1}$ (GHz)	$f_{p,1}$ (GHz)	$\gamma_{s,1}/(2\pi)$ (MHz)	$f_{s,2}$ (GHz)	$f_{p,2}$ (GHz)	$\gamma_{s,2}/(2\pi)$ (MHz)
0.8445±0.0001	0.9272±0.0003	29.0±0.2	1.0211±0.0003	1.0325±0.0003	24.0±0.5

then repeated for the $|S_{11}|$ curve measured from the $N = 4$ array of SRRs and 3/16-inch aluminum cut wires. For this fit, we fixed the values of k_{sc} and $L_{1,sc}$ to be 1.54 and 1.1339, respectively. The measured $|S_{11}|$ curve and obtained fit for this NIM are presented in Fig. 7.6(b). Additionally, the obtained best fit parameters are shown in Table 7.2.

Table 7.2: Best fit parameters for one-loop-one-gap resonator filled with four SRRs and four 3/16-inch diameter aluminum cut wires.

$f_{s,1}$ (GHz)	$f_{p,1}$ (GHz)	$\gamma_{s,1}/(2\pi)$ (MHz)	$f_{s,2}$ (GHz)	$f_{p,2}$ (GHz)	$\gamma_{s,2}/(2\pi)$ (MHz)
0.8520±0.0002	0.9298±0.0003	30.2±0.3	1.0254±0.0003	1.0365±0.0004	23.2±0.5

From the parameters obtained from the fits, we are able to find the relative effective permeability of our array by plotting Eqs. (7.1) and (7.2). The resulting plots of both μ', the permeability's real component, and μ'', the permeability's imaginary component, are shown for both $N = 4$ arrays of Teflon rods with SRRs and aluminum cut wires with SRRs in Fig. 7.7. By analyzing Fig. 7.7, we can see that the addition of aluminum (as

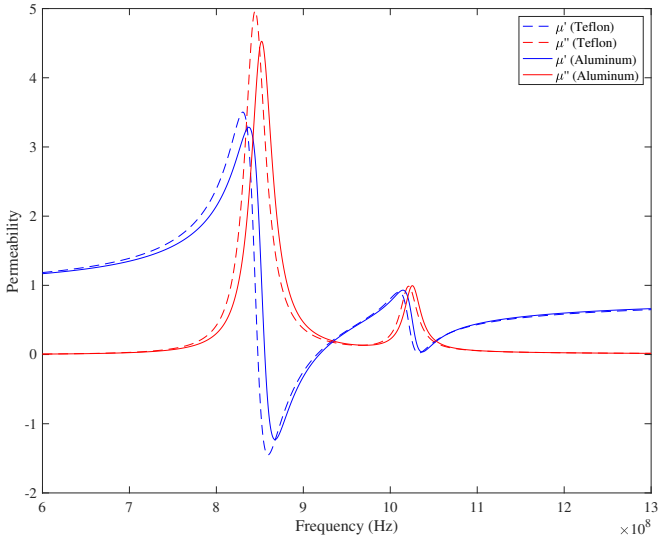

Figure 7.7: The relative effective permeability for one-dimensional arrays of four Teflon rods and four SRRs compared with four aluminum cut wires and four SRRs.

shown by the solid line plots) had little effect on the permeability of arrays of just SRRs (as shown by the dashed line plots). In fact, the permeability of our NIM is almost entirely due to SRRs and that the cut wires provide only small perturbation, which is essentially negligible. Permeability defines the magnetization a given material gains from a magnetic field [5]. Thus, as cut wire arrays are only expected to produce an electric response, and thus modify the permittivity, it was expected their addition to the SRR array would have a minimal effect on its permeability. Another important result from Fig. 7.7 is that μ'' is found to be always positive. This implies power loss, rather than the power gain some previous research has predicted, in the NIM [14].

Chapter 8

Further Investigations

8.1 Applying Current to Cut Wire Arrays

Throughout all of of these measurements, the LGR's bore has only been exposed to the uniform magnetic field induced from the AC signal supplied to the coupling loop while the electric field has remained at approximately zero. An area for further research is to investigate the effect of supplying the cut wires within the LGR's bore with current. This, in turn, is expected to vary the LGR bore's magnetic field. In principle, this allows us to artificially mimic the effect of an electric field within the cut wires, while the LGR's bore still experiences a purely magnetic field. For the preliminary steps of this investigation, we have designed the experimental set-up displayed in Fig. 8.1.

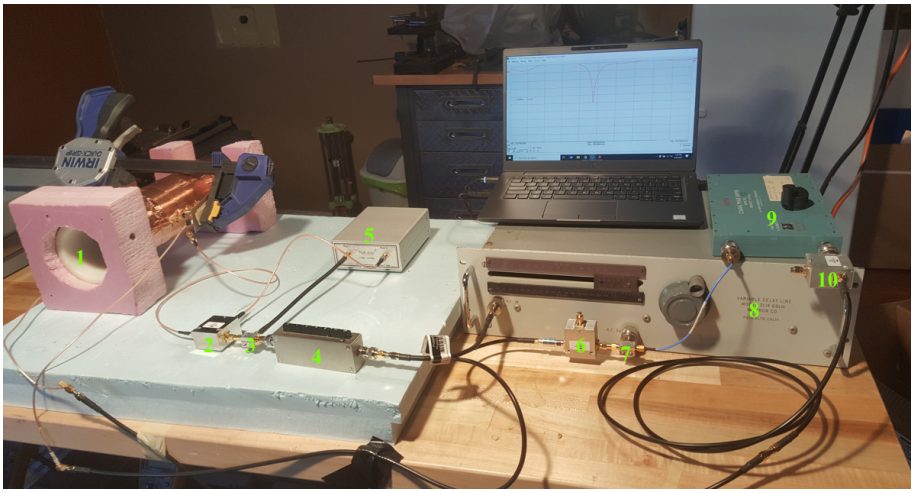

Figure 8.1: Initial experimental set-up for applying current to cut wire arrays. The following equipment is labelled: 1 is an EM shield containing the LGR; 2,6, and 10 are circulators; 3 and 7 are power splitters, 4 is an attenuator; 5 is a VNA; 8 and 9 are phase shifters.

Figure 8.1 shows an EM shield (1) which contains a one-loop-one-gap resonator. In order to apply current to the cut wires within the resonator's bore, the wires were cut to be long enough to be accessible from outside of the EM shield. To secure these wires, three holes, one for each wire, were drilled through both sides of the LGR and EM shield. Then, we secured copper electrodes to each end of the wires using a clamp. In order to avoid direct contact with the aluminum LGR, we wrapped masking tape around each cut wire where it passed through the LGR's shell. The EM shield was used to prevent the

LGR from interacting with the outer portion of the cut wires and also limit other radiative losses due to the laboratory surroundings [21]. Again, the VNA (5) was used as a power source. The transmitting port of the VNA supplied an AC current to a power splitter (3), which directed half of the signal to a circulator (2) and the other half through an attenuator (4). The signal supplied to port 1 of the circulator (2) was transmitted to the coupling loop of the LGR via port 2. Then, the signal reflected back to port 2 was passed to the receiving port of the VNA via port 3 of the circulator. The other half of the signal travelled through the attenuator (4) and was supplied to a phase shifter (8). From here, the signal was split again at the second power splitter (6). Then half of the remaining signal was directed through a circulator (6) and set to power the copper electrode on the right hand side of the EM shield. The other half of the signal was directed through another phase shifter (9) and circulator (10) before it powered the left copper electrode.

The first phase shifter (8) functioned to adjust the phase of the current in the wires relative to the oscillating magnetic field in the bore of the resonator. The second phase shifter (9), was used to set the desired phase of the signals supplied to the copper electrodes. The signal supplied to the left electrode was set to be 180°s out of phase with the right electrodes signal. Thus, while one AC signal was at its maximum, the other was at its minimum, and they crossed zero simultaneously. This experimental set-up allowed us to control the phase of the signals being delivered to the copper electrodes and thus to the cut wire array.

By supplying a current through the cut wires, a magnetic field will be induced which circles the wires. This is expected to result in a non-uniform magnetic field within the LGR bore which will allow us to further explore the permeability of the cut wire array. Ultimately, we predict that we may observe a negative imaginary component of the effective relative permeability, μ'', for specific phases of the current in the cut wires relative to the oscillating magnetic field.

8.2 Incorporating Other Metamaterials

Another aspect a future project could investigate is the incorporation of other metamaterials. Specifically, we could make use of complementary split-ring resonators (CSRRs), the dual of the SRR [22]. This structure was originally proposed in 2004 by Falcone *et al.* and was created to provide the negative permittivity component of an NIM array. These CSRRs essentially act as a single electric dipole with negative polarizability. They composed their CSRRs by etching out SRR like dimensions into a planar circuit board and a thin metallic plate [23]. CSRRs are quite compact and thus may be easier to work with than cut wires for higher dimension NIM arrays.

Chapter 9

Conclusion

The complex permeability, $\mu_r = \mu' - j\mu''$, of metamaterials was characterized using LGRs. The metamaterials we worked with included SRR arrays, which have a negative permeability over a small range of microwave frequencies just above their resonant frequency, as well as cut wire arrays, which are designed to have a negative permittivity at microwave frequencies. To characterize these arrays, the experimental procedure presented by S. L. Madsen and J. S. Bobowski to measure the permeability of SRR arrays was adapted to incorporate arrays of cut wires as well as arrays of SRRs and cut wires [6]. The motivation behind this project was to explore the effect the addition of cut wires has to the permeability of an array of SRRs. Previous investigations, including numerical simulations and experimental measurements, have suggested that the imaginary component of the permeability is negative for cut wire arrays [6] [7]. This is an unphysical result as it describes power gain in the metamaterial.

To determine the permeability of these metamaterials, LGRs were used. An SMA cable connected the LGR's coupling loop to a VNA. This allowed us to supply a signal to and extract the reflection coefficient, $|S_{11}|$, from the LGR's bore. In order to model $|S_{11}|$, we represented the LGR as an LRC circuit. From here, Kirchhoff's voltage law was applied to find the effective impedance of the LGR which was used to model the expected $|S_{11}|$ curve [5] [19]. However, as the LGR bore was loaded with magnetic material, the expected $|S_{11}|$ curve varied as the bore's inductance varied. To account for this, we used Pendry *et al.*'s model for the permeability of SRR arrays which accounts for the frequency dependence of permeability [1].

Initially, we measured the $|S_{11}|$ curves for arrays of aluminum cut wires. Overall, we qualitatively observed minimal and non-systematic changes in the produced $|S_{11}|$ reflections for arrays comprised of various numbers of cut wires. Thus, as $|S_{11}|$ depends on the permeability of the material loaded inside the LGR's bore, the addition of cut wires had a very small effect on the bore's permeability. Lastly, we measured $|S_{11}|$ for arrays containing both SRRs and cut wires. Using the model we derived for $|S_{11}|$, we extracted the resonant frequency, magnetic plasma frequency, and damping constant for arrays of SRRs and arrays of both SRRs and cut wires. From these parameters, we plotted the relative effective permeability of the arrays and found that the addition of aluminum cut wires had little effect on the permeability of arrays of solely SRRs. In fact, the permeability if the metamaterial was almost entirely due to SRRs. This was anticipated as the cut wires are expected to only provide an electric response. Moreover, the imaginary component, μ'', of the permeability of the array was found to be positive over the entire frequency range which is expected for power dissipation in the metamaterial.

Bibliography

[1] J. B. Pendry, A. J. Holden, D. J. Robbins, and W. J. Stewart, "Magnetism from conductors and enhanced nonlinear phenomena," *IEEE Transactions on Microwave Theory and Techniques*, vol. 47, no. 11, pp. 2075–2084, 1999.

[2] R. S. Kshetrimayum, "A brief introduction to metamaterials," *IEEE Potentials*, vol. 23, no. 5, pp. 44–46, 2004.

[3] J. B. Pendry, "Negative refraction," *Contemporary Physics*, vol. 45, no. 3, pp. 191–202, 2004.

[4] V. G. Veselago, "The electrodynamics of substances with simultaneously negative values of ε and μ," *Soviet Physics Uspekhi*, vol. 10, no. 4, pp. 509–514, 1968.

[5] D. J. Griffiths, *Introduction to Electrodynamics*. Pearson, 4th ed., 2012.

[6] S. L. Madsen and J. S. Bobowski, "The complex permeability of split-ring resonator arrays measured at microwave frequencies," *IEEE Transactions on Microwave Theory and Techniques*, vol. 68, no. 8, pp. 3547–3557, 2020.

[7] T. Koschny, P. Markoš, D. R. Smith, and C. M. Soukoulis, "Resonant and antiresonant frequency dependence of the effective parameters of metamaterials," *Phys. Rev. E*, vol. 68, no. 6, 2003.

[8] J. B. Pendry, "Negative refraction makes a perfect lens," *Physical Review Letters*, vol. 85, no. 18, pp. 3966–3969, 2000.

[9] D. Schurig, J. J. Mock, B. J. Justice, S. A. Cummer, A. F. S. J. B. Pendry, and D. R. Smith, "Metamaterial electromagnetic cloak at microwave frequencies," *Science*, vol. 314, no. 5801, pp. 977–980, 2006.

[10] A. R. Djordjevic, R. M. Biljie, V. D. Likar-Smiljanic, and T. K. Sarkar, "Wideband frequency-domain characterization of fr-4 and timedomain causality," *IEEE Trans. Electromagn. Compat.*, vol. 43, no. 4, pp. 662–667, 2001.

[11] S. I. Maslovski, S. A. Tretyakov, and P. A. Belov, "Wire media with negative effective permittivity: A quasi-static model," *Microwave and Optical Technology Letters*, vol. 35, no. 1, pp. 47–50, 2002.

[12] P. G. García and J. Fernández-Álvarez, "Floquet-bloch theory and its application to the dispersion curves of nonperiodic layered systems," *Mathematical Problems in Engineering*, 2015.

[13] J. Zhou, *Study of left-handed materials*. PhD thesis, Iowa State University, 2008.

[14] J. S. Bobowski, "Probing split-ring resonator permeabilities with loop-gap resonators," *Can. J. Phys.*, vol. 96, p. 878–886, 2018.

[15] J. S. Bobowski, "Using split ring resonators to measure the electromagnetic properties of materials: An experiment for senior physics undergraduates," *Am. J. Phys.*, vol. 81, no. 12, pp. 899–904, 2013.

[16] W. M. Haynes, *CRC Handbook of Chemistry and Physics*. 95th ed., 2014-2015.

[17] G. A. Rinard, R. W. Quine, S. S. Eaton, and G. R. Eaton, "Microwave coupling structures for spectroscopy," *Journal of Magnetic Resonance*, vol. 105, pp. 3137–3144, 1993.

[18] D. L. Eggleston, *Basic Electronics for Scientists and Engineers*. Cambridge University Press, 2011.

[19] M. Steer, *Microwave and RF Design: Transmission Lines*. NC State University, 3rd ed., 2019.

[20] S. Pfenninger, W. Froncisz, J. Forrer, J. Luglio, and J. S. Hyde, "General method for adjusting the quality factor of epr resonators," *Rev. Sci. Instrum.*, vol. 66, no. 10, pp. 4857–4865, 1995.

[21] J. S. Bobowski and H. Nakahara, "Design and characterization of a novel toroidal split-ring resonator," *Review of Scientific Instruments*, vol. 87, 2016.

[22] H. Bahrami, M. Hakkak, and A. Pirhadi, "Using complementary split ring resonators (csrr) to design bandpass waveguide filters," *Asia-Pacific Microwave Conference*, pp. 1–4, 2017.

[23] F. Falcone, T. Lopetegi, M. Laso, J. Baena, J. Bonache, M. Beruete, R. Marques, F. Martín, and M. Sorolla Ayza, "Babinet principle applied to the design of metasurfaces and metamaterials," *Physical review letters*, vol. 93, no. 19, pp. 1–4, 2004.

Appendix A

$|S_{11}|$ Measurements of $1 \times 1 \times N$ NIM Arrays

Appendix A contains the remaining experimental $|S_{11}|$ curves plotted as a function of frequency for $1 \times 1 \times N$ arrays of SRRs and 3/16-inch or 1/8-inch aluminum cut wires or Teflon rods. Measurements were taken using the one-loop-one-gap resonator.

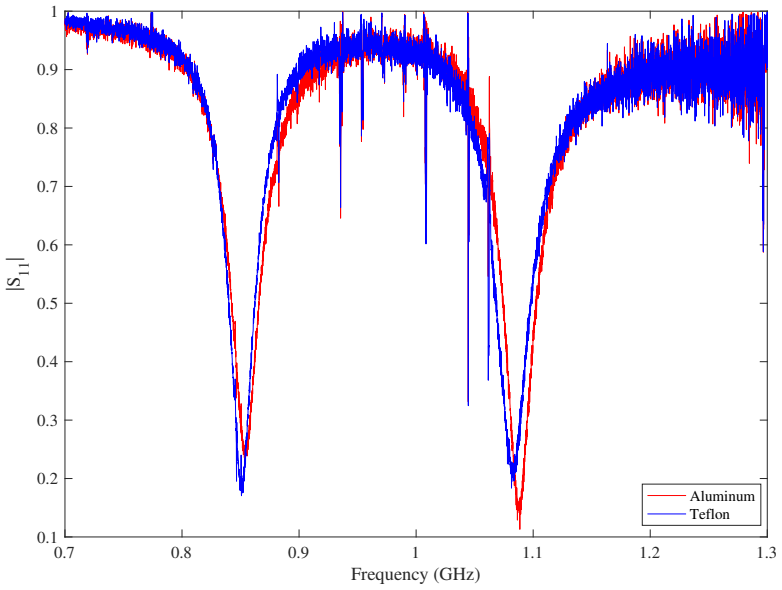

Figure A.1: $|S_{11}|$ as a function of frequency when a single SRR and one 3/16-inch diameter aluminum cut wire (shown in red) or one 3/16-inch diameter Teflon rod (shown in blue) are loaded in the bore of the LGR.

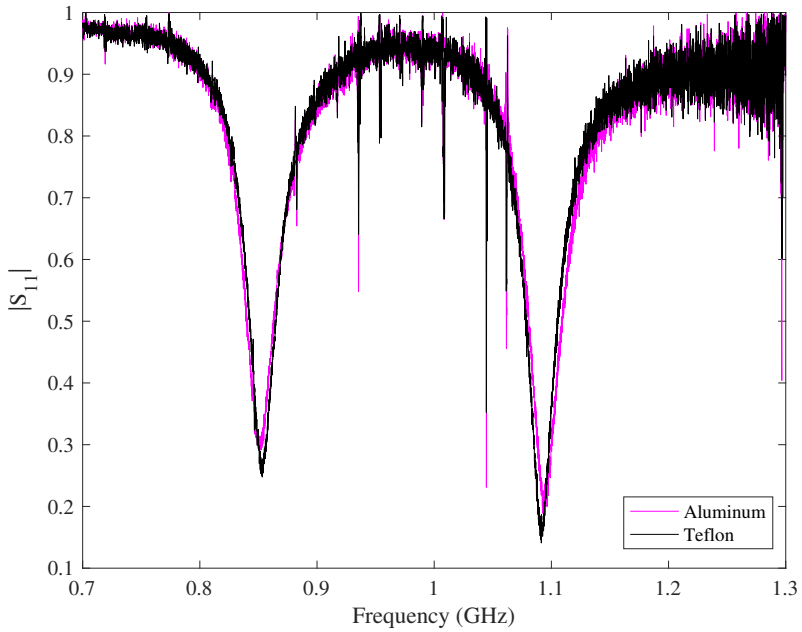

Figure A.2: $|S_{11}|$ as a function of frequency when a single SRR and one 1/8-inch diameter aluminum cut wire (shown in magenta) or one 1/8-inch diameter Teflon rod (shown in black) are loaded in the bore of the LGR.

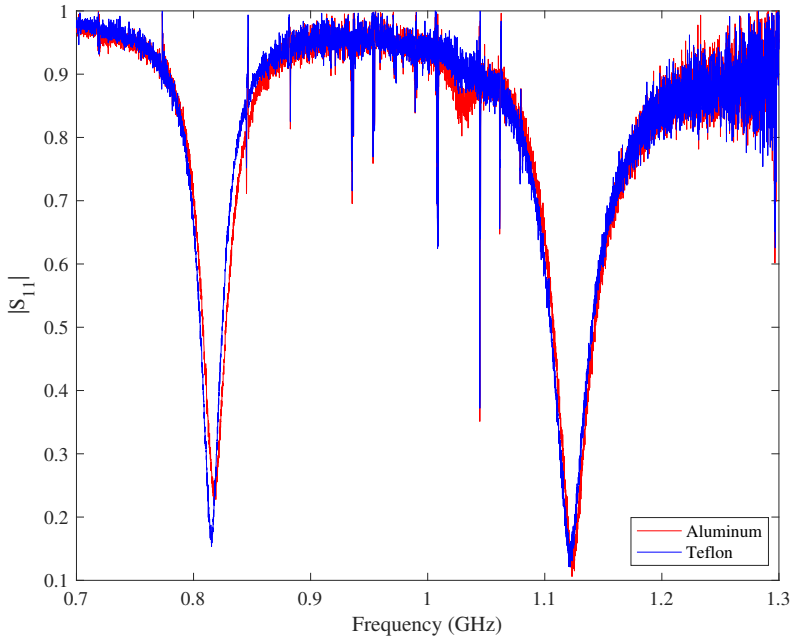

Figure A.3: $|S_{11}|$ as a function of frequency when two SRRs and two 3/16-inch diameter aluminum cut wires (shown in red) or two 3/16-inch diameter Teflon rods (shown in blue) are loaded in the bore of the LGR.

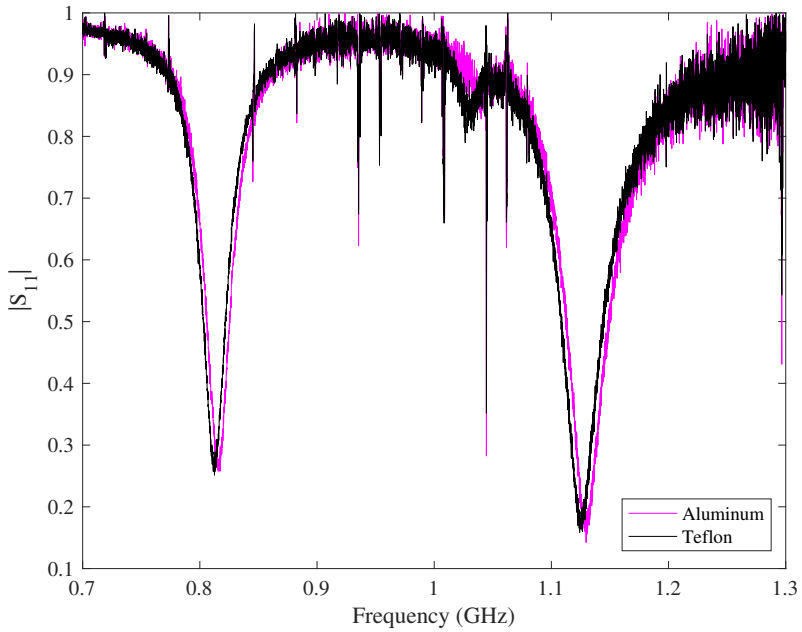

Figure A.4: $|S_{11}|$ as a function of frequency when two SRRs and two 1/8-inch diameter aluminum cut wires (shown in magenta) or two 1/8-inch diameter Teflon rods (shown in black) are loaded in the bore of the LGR.

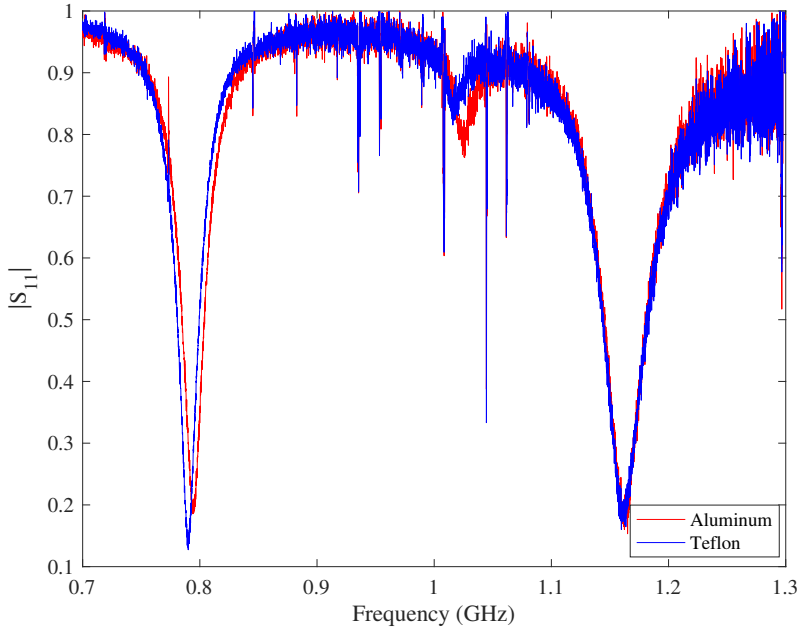

Figure A.5: $|S_{11}|$ as a function of frequency when three SRRs and three 3/16-inch diameter aluminum cut wires (shown in red) or two 3/16-inch diameter Teflon rods (shown in blue) are loaded in the bore of the LGR.

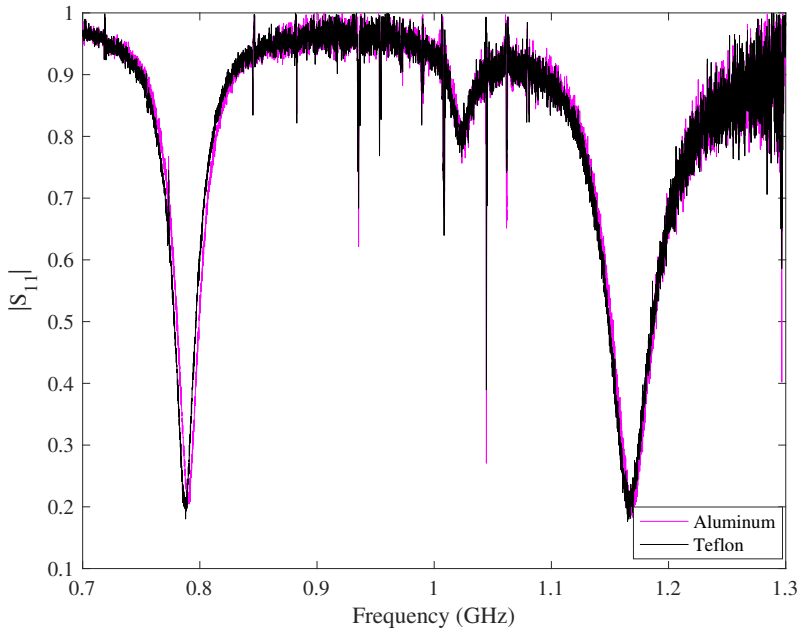

Figure A.6: $|S_{11}|$ as a function of frequency when three SRRs and three 1/8-inch diameter aluminum cut wires (shown in magenta) or three 1/8-inch diameter Teflon rods (shown in black) are loaded in the bore of the LGR.

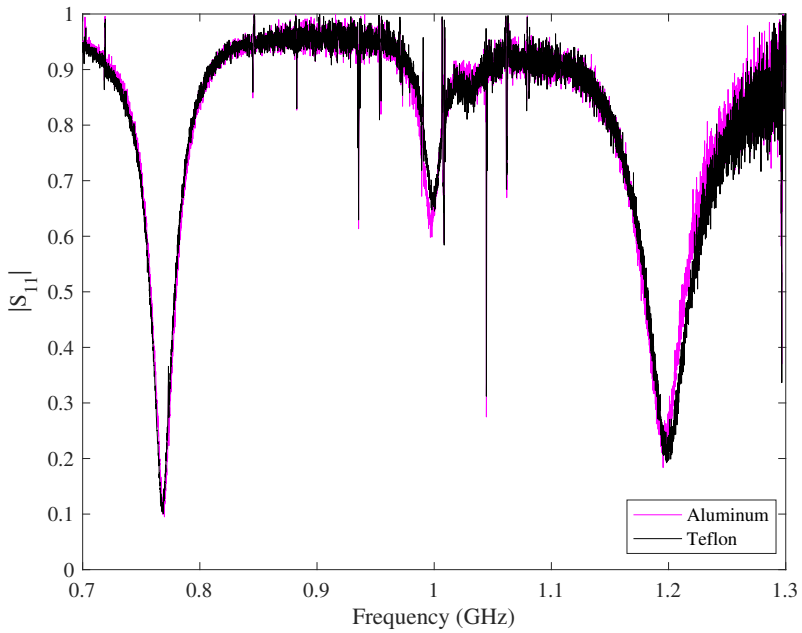

Figure A.7: $|S_{11}|$ as a function of frequency when four SRRs and four 1/8-inch diameter aluminum cut wires (shown in magenta) or four 1/8-inch diameter Teflon rods (shown in black) are loaded in the bore of the LGR.

Appendix B

$|S_{11}|$ Measurements of $2 \times 2 \times N$ NIM Arrays

Appendix B contains the remaining experimental $|S_{11}|$ curves plotted as a function of frequency for $2 \times 2 \times N$ arrays of SRRs and 3/16-inch or 1/8-inch aluminum cut wires or Teflon rods. Measurements were taken using the two-loop-one-gap resonator.

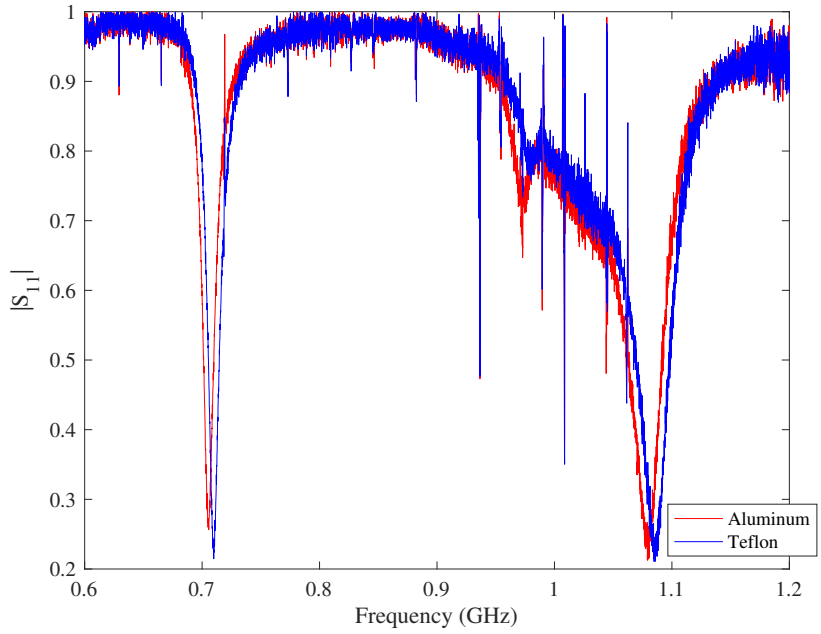

Figure B.1: $|S_{11}|$ as a function of frequency when four SRRs and four 1/8-inch diameter aluminum cut wires (shown in magenta) or four 1/8-inch diameter Teflon rods (shown in black) are loaded in the bore of the LGR.

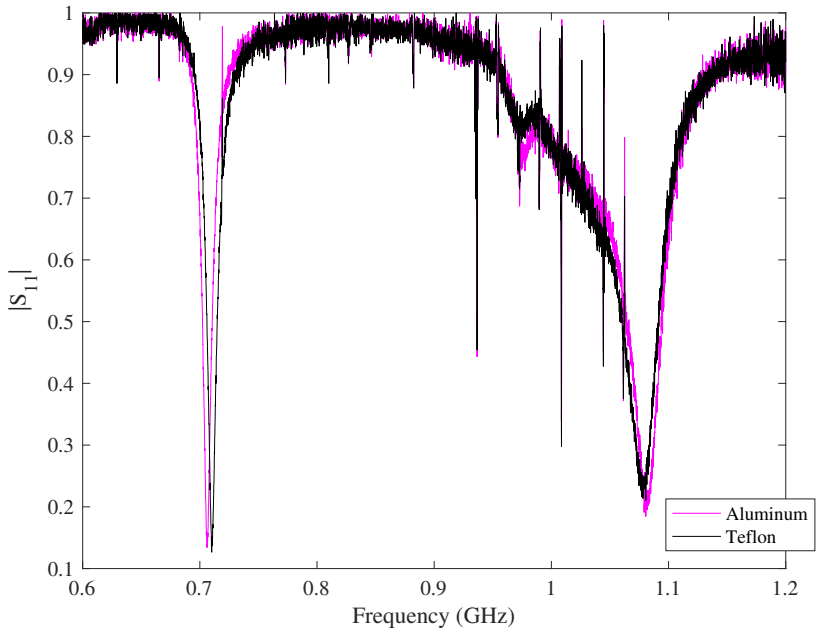

Figure B.2: $|S_{11}|$ as a function of frequency when a four SRR and four 1/8-inch diameter aluminum cut wires (shown in magenta) or four 1/8-inch diameter Teflon rods (shown in black) are loaded in the bore of the LGR.

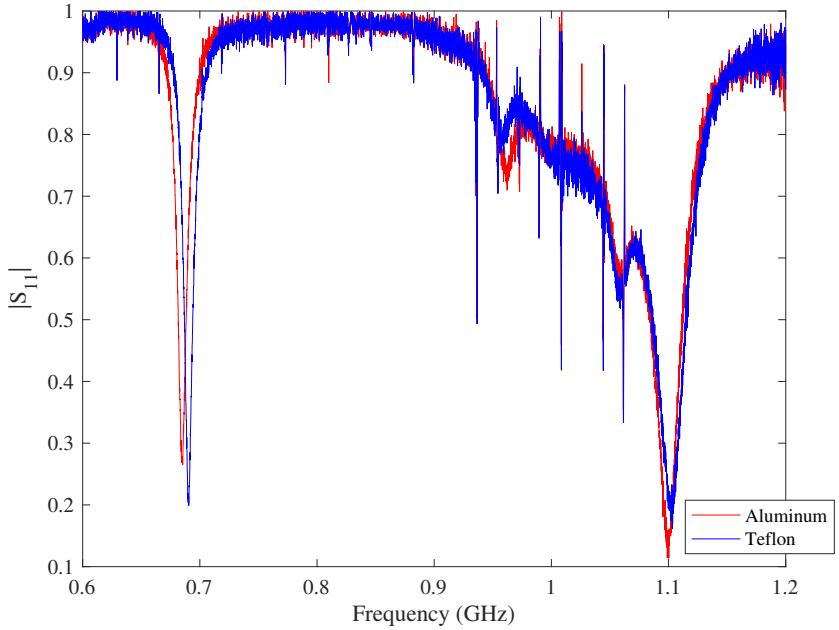

Figure B.3: $|S_{11}|$ as a function of frequency when eight SRRs and eight 3/16-inch diameter aluminum cut wires (shown in red) or eight 3/16-inch diameter Teflon rods (shown in blue) are loaded in the bore of the LGR.

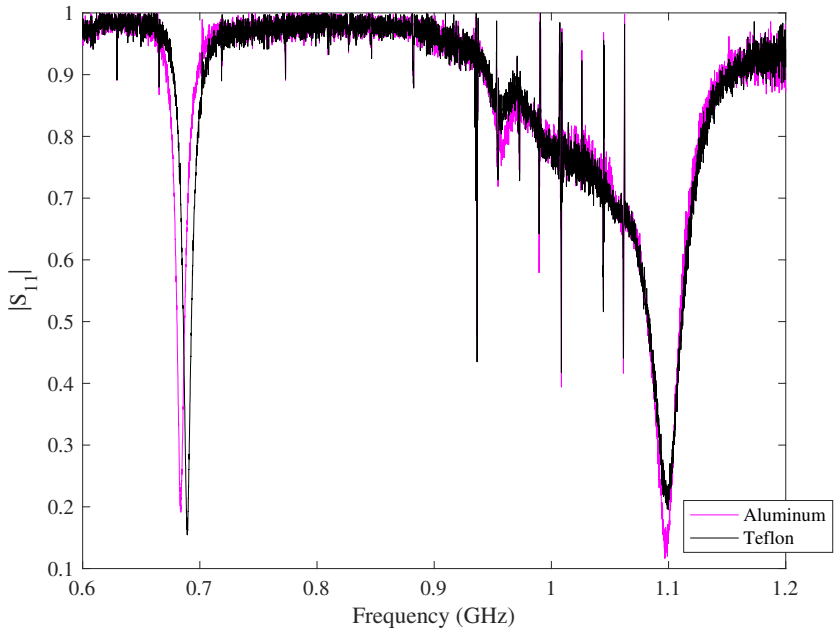

Figure B.4: $|S_{11}|$ as a function of frequency when eight SRRs and eight 1/8-inch diameter aluminum cut wires (shown in magenta) or eight 1/8-inch diameter Teflon rods (shown in black) are loaded in the bore of the LGR.

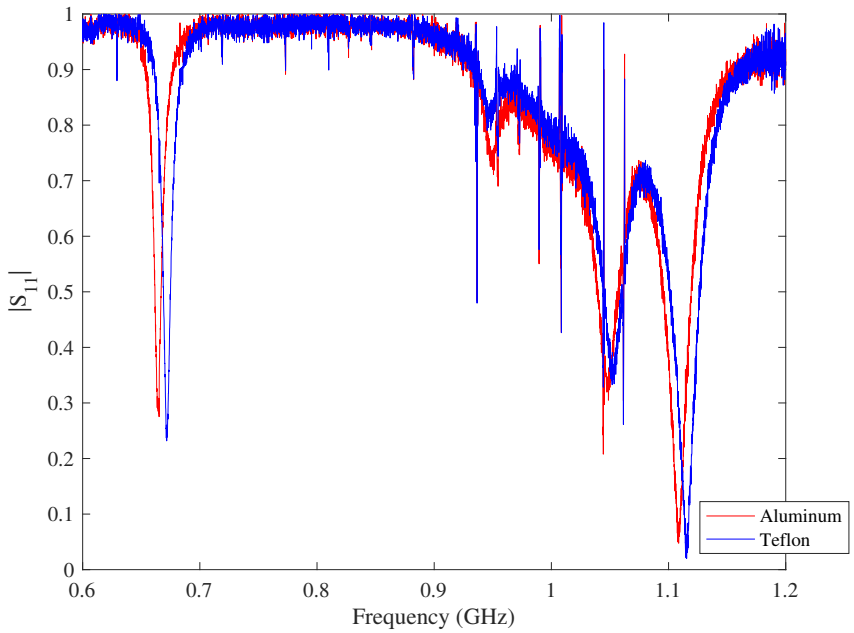

Figure B.5: $|S_{11}|$ as a function of frequency when twelve SRRs and twelve 3/16-inch diameter aluminum cut wires (shown in red) or twelve 3/16-inch diameter Teflon rods (shown in blue) are loaded in the bore of the LGR.

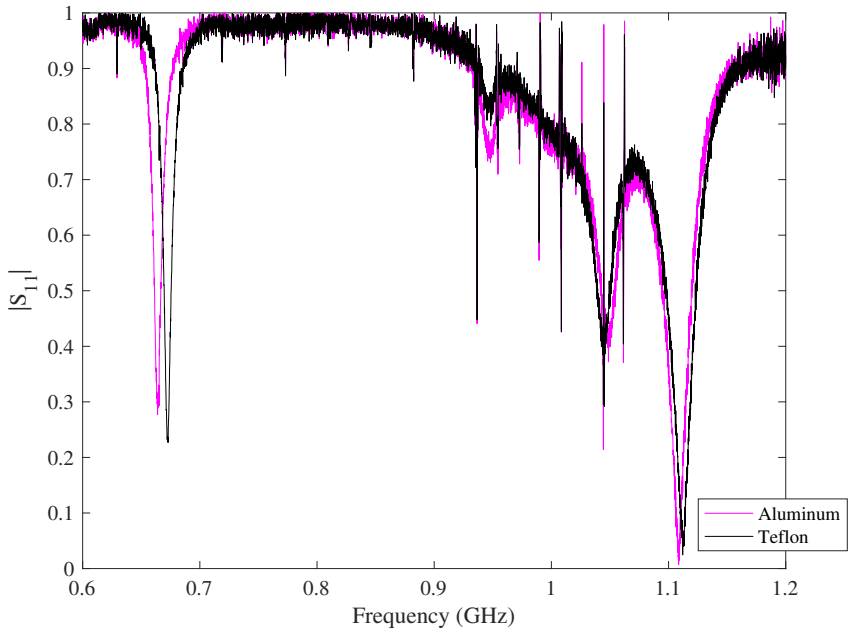

Figure B.6: $|S_{11}|$ as a function of frequency when twelve SRRs and twelve 1/8-inch diameter aluminum cut wires (shown in magenta) or twelve 1/8-inch diameter Teflon rods (shown in black) are loaded in the bore of the LGR.

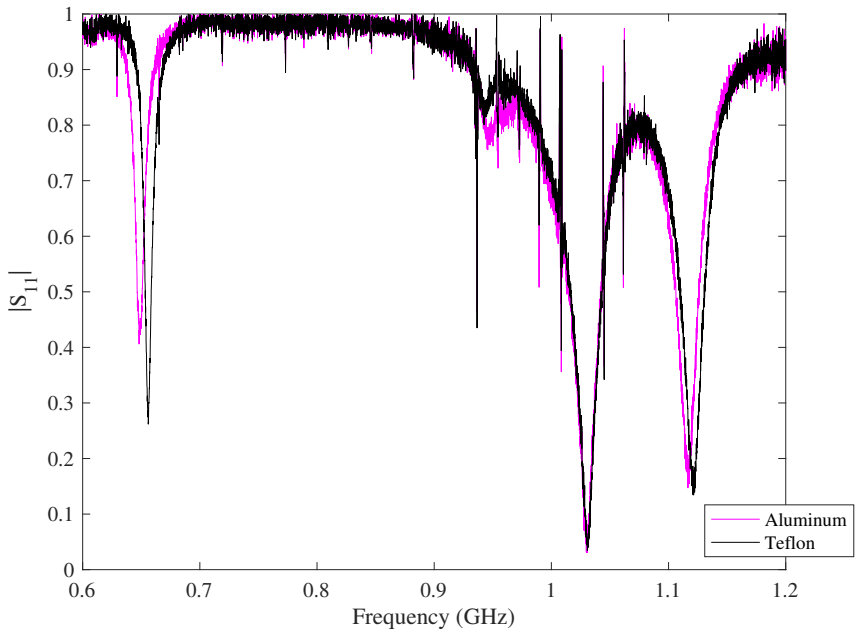

Figure B.7: $|S_{11}|$ as a function of frequency when sixteen SRRs and sixteen 1/8-inch diameter aluminum cut wires (shown in magenta) or sixteen 1/8-inch diameter Teflon rods (shown in black) are loaded in the bore of the LGR.

Appendix C

$|S_{11}|$ MATLAB Fit for Arrays of NIMs

Appendix C contains the MATLAB code used to fit the $|S_{11}|$ curves measured from a one-loop-one-gap LGR partially filled with magnetic material. This fit makes use of Pendry *et al.*'s model for SRR permeability, as given by Eqs. (7.1) and (7.2), as well as the model derived for effective impedance of a partially filled bore, as given by Eqs. (6.11) to (6.14). These equations are used in conjunction with Eq. (4.12) to fit the experimentally measured $|S_{11}|$ curves. This specific fit was done for an $N = 4$ 1-D array of 3/16-inch diameter aluminum cut wires and SRRs.

```
% Ava Cornell
% February 15, 2021
% Modified from:
% Jake Bobowski
% January 12, 2021
% Try entering the fit function for a LGR with its bore
% partially loaded with a single SRR and cut wire.
clearvars;
format longE;

% First, enter the real and imaginary parts of the relative permeability.
% Use the model proposed by Pendry.  However, it is possible
% to also use the Lorenztian model.  Note also that one can sum create a
% superposition of these relative permeabilities to caputre additional
% features present in the data.  This superposition should still obey the
% Kramers–Kronig relation between the real and imaginary parts.

% Start will a range of frequencies
fstart = 700e6; % Hz
fstop = 1300e6; % Hz
f = linspace(fstart, fstop, 5000);

```

```
% Enter some parameters for Pendry's permeability model. Values from Table 2 of "The
% Complex Permeability of Split-Ring Resonator Arrays Measured at Microwave Frequencies" by Madsen and Bobowski.
fs1 = 850e6; % Hz
fp1 = 930e6; % Hz
gS1 = 33*1e6; % Hz
g1 = gS1*(f/fs1).^(0.5);
fs2 = 1015e6; % Hz
fp2 = 1031e6; % Hz
gS2 = 11*1e6; % Hz
g2 = gS2*(f/fs2).^(0.5);
mu1 = 1 - (1 - (fs1/fp1)^2)*(1 - (fs1./f).^2)./((1 - (fs1./f).^2).^2 + (g1./f).^2)- (1 - (fs2/fp2)^2)*(1 - (fs2./f).^2)./((1 - (fs2./f).^2).^2 + (g2./f).^2);
mu2 = (g1./f)*(1 - (fs1/fp1)^2)./((1 - (fs1./f).^2).^2 + (g2./f).^2)+(g2./f)*(1 - (fs2/fp2)^2)./((1 - (fs2./f).^2).^2 + (g2./f).^2);

% Plot the relative permeability components
%plot(f, mu1, 'r');
%hold on;
%plot(f, mu2, 'b');
%hold off;
%figure;

% Now enter the scaled inductance (\ell) of the partially-filled LGR bore.
% These expressions should correspond Eqs. (6.11) and (6.12).
N = 4;
spacer = 20.32;
thickness = 1.54;
LGRlength = 112.00;
x = N*(spacer + thickness)/(LGRlength); % x is the filling factor
murSq = mu1.^2 + mu2.^2;
l1 = (mu1*x + murSq*(1 - x))./((x + mu1*(1 - x)).^2 + mu2.^2*(1 - x)^2);
l2 = mu2*x./((x + mu1*(1 - x)).^2 + mu2.^2*(1 - x)^2);

% Plot the scaled inductance components
%figure;
%plot(f, l1, 'r');
%hold on;
```

```
%plot(f, l2, 'b');
%plot(f, lmag, 'g');
%hold off;

% OK, now enter the expressions needed to construct the impedance of the
% coupled LGR with its bore partially-loaded with a SRR/cut wire
% array.
f0 = 857.7e6; % Hz
Q0 = 49.08;

% Here, then, is the impedance of an inductively couple two-loop, one-gap
% LGR with one of its bores partially loaded with a SRR array. These
% expressions should correspond to Eqs. (6.13) and (6.14).
L1 = 42.54e-9; % Henries
k = 0.3;
R1 = (2*pi*f*L1).*(f/f0).*k^2.*((l1/Q0).*(f/f0).^0.5 + l2.*(f0./f))./(((1/Q0)*(f/f0).^0.5 + (f/f0).*l2).^2 + ((f/f0).*l1 - f0./f).^2);
X1 = 2*pi*f*L1.*(1 - (f/f0)*k^2.*(l2.*((1/Q0)*(f/f0).^0.5 + l2.*(f/f0)) + l1.*(l1.*(f/f0) - f0./f))./(((1/Q0)*(f/f0).^0.5 + (f/f0).*l2).^2 + ((f/f0).*l1 - f0./f).^2));
Z1mag = (R1.^2 + X1.^2).^0.5;

% Plot the impedance components
%figure;
%plot(f, R1, 'r');
%hold on;
%plot(f, X1, 'b');
%plot(f, Z1mag, 'g');
%hold off;

% Now calculate the reflection coefficient S11
Z0 = 50;
offSlope = 40.8e9;

ReS11 = ((Z1mag/Z0).^2 - 1)./(((Z1mag/Z0).^2 + 1) + 2*R1/Z0);
ImS11 = 2*(X1/Z0)./(((Z1mag/Z0).^2 + 1) + 2*R1/Z0);
S11mag = (ReS11.^2 + ImS11.^2).^0.5 - f/offSlope;

% Plot the reflection coefficents
%figure;
```

```
95 %plot(f, ReS11, 'r');
96 %hold on;
97 %plot(f, ImS11, 'b');
98 %plot(f, S11mag, 'g');
99 %hold off;
100
101
102 % Import the data and plot it with the calculated reflection
       coefficient.  Try
103 % adjusting the permeability parameters until the calculated S11
104 % approximately matches the measured S11.
105 M = dlmread('one-loop one-gap LGR - 4 SRRs - 4 Aluminum rods.txt
       ');
106 fdata = M(:,4)';
107 S11 = M(:,5)';
108
109 figure;
110 plot(f, S11mag, 'r');
111 hold on;
112 plot(fdata, S11, 'ko');
113 hold off;
114
115
116 % This stop is used to stop the program.  If you are just
       adjusting
117 % parameter values to try to find good starting values,
       uncomment the stop
118 % below.  If you'd like to actually do the best-fit, then
       comment out the
119 % stop.
120
121 %stop;
122 clearvars;
123
124 % Enter the value of the filling factor.
125 N = 4;
126 spacer = 20.32;
127 thickness = 1.54;
128 LGRlength = 112.00;
129 x = N*(spacer + thickness)/(LGRlength);
130
131
132 % Import the data.
```

```
133 M = dlmread('one-loop one-gap LGR - 4 SRRs - 4 Aluminum rods.txt
    ');
134 fdata = M(:,4)';
135 S11 = M(:,5)';
136
137
138 % The fit parameters will be b(1), b(2), b(3), ...
139 syms f
140 b = sym('b', [1 6]);
141 % b(1) = fs1 (GHz)
142 % b(2) = fp1 (GHz)
143 % b(3) = gS1 (MHz)
144 % b(4) = fs2 (GHz)
145 % b(5) = fp2 (GHz)
146 % b(6) = gS2 (MHz)
147 % b(7) = offSlope (GHz)
148
149 % Now enter the expressions for mu1 (real part) and mu2 (
    imaginary part).
150 % Insert the appropriate fit parameter symbols in place of fsm
    fpm and g.
151 g1 = sqrt(b(3)^2)*1e6*(f/(b(1)*1e9)).^(0.5);
152 g2 = sqrt(b(6)^2)*1e6*(f/(b(4)*1e9)).^(0.5);
153 mu1 = 1 - ((1-(b(1)./(b(2))).^2).*(1-((b(1)*1e9)./f).^2))
    ./((1-((b(1)*1e9)./f).^2).^2+(g1./f).^2)-((1-(b(4)./(b(5)))
    .^2).*(1-((b(4)*1e9)./f).^2))./((1-((b(4)*1e9)./f).^2).^2+(g2
    ./f).^2);
154 mu2 = ((g1./f).*(1-(b(1)./(b(2))).^2))./((1-((b(1)*1e9)./f).^2)
    .^2.+(g1./f).^2)+((g2./f).*(1-(b(4)./(b(5))).^2))./((1-((b(4)
    *1e9)./f).^2).^2.+(g2./f).^2);
155
156 % Now enter the expressions for l1 (real part) and l2 (imaginary
     part).
157 l1 = (mu1.*(x + mu1*(1 - x)) + mu2.^2*(1 - x))./((x + mu1*(1 - x
    )).^2 + mu2.^2*(1 - x)^2);
158 l2 = mu2*x./((x + mu1*(1 - x)).^2 + mu2.^2*(1 - x)^2);
159 lmag = (l1.^2 + l2.^2).^0.5;
160
161 % Enter values for L1, f0, Q0, and k previously determined form
    fits to the
162 % empty-bore LGR. L1 and k estimated for this specific fit.
163 L1 = 42.54*1e-9*1.1339;
164 f0 = 0.8577*1e9;
165 Q0 = 49.08;
```

```
166 k = 0.3*1.54;
167
168 % Now enter the expressions for R and X, the real and imaginary
      components of the impedance of the coupled LGR
169 % with a partially-filled bore.
170 R1 = (2*pi*f*L1).*(f/f0).*k^2.*((l1/Q0).*(f/f0).^0.5 + l2.*(f0./
      f))./(((1/Q0)*(f/f0).^0.5 + (f/f0).*l2).^2 + ((f/f0).*l1 - f0
      ./f).^2);
171 X1 = 2*pi*f*L1.*(1 - (f/f0)*k^2.*(l2.*((1/Q0)*(f/f0).^0.5 + l2
      .*(f/f0)) + l1.*(l1.*(f/f0) - f0./f))./(((1/Q0)*(f/f0).^0.5 +
       (f/f0).*l2).^2 + ((f/f0).*l1 - f0./f).^2));
172 Z1mag = (R1.^2 + X1.^2).^0.5;
173
174 % Here are the expression for calculating S11 from R and X.  the
      offSlope
175 % parameter is used to take into account losses associated with
      the lengths
176 % of coaxial cable that lead up to the coupling loop.  These
      losses grow as
177 % frequnecy increases.
178 Z0 = 50;
179 offSlope = 40.8*1e9;
180 ReS11 = ((Z1mag/Z0).^2 - 1)./(((Z1mag/Z0).^2 + 1) + 2*R1/Z0);
181 ImS11 = 2*(X1/Z0)./(((Z1mag/Z0).^2 + 1) + 2*R1/Z0);
182 S11mag = (ReS11.^2 + ImS11.^2).^0.5 - f/offSlope;
183
184 % We now define the model function required for MATLAB's fitting
      routine
185 % fitnlm.
186 S11fcn = matlabFunction(S11mag);
187 mdlS11 = @(b,f) S11fcn(b(1), b(2), b(3), b(4), b(5), b(6), f);
188
189 % Here, we call the fitting routine and provide some intitial
      parameter
190 % estimates.
191 res = fitnlm(fdata,S11,mdlS11,[0.85, .930, 33, 1.015, 1.031,
      11])
192
193 % Extract the best-fit paramters.
194     fs1 = res.Coefficients.Estimate(1);
195     fp1 = res.Coefficients.Estimate(2);
196     gS1 = res.Coefficients.Estimate(3);
197     fs2 = res.Coefficients.Estimate(4);
198     fp2 = res.Coefficients.Estimate(5);
```

```
199     gS2 = res.Coefficients.Estimate(6);
200     %offSlope = res.Coefficients.Estimate(7);
201
202 % Put the paramter values into a list.
203 param = [fs1, fp1, gS1, fs2, fp2, gS2];
204 param'
205
206 % A bunch of frequency values
207 xx = linspace(min(fdata) - 10e7, max(fdata), 5000);
208
209 % Plot the S11 data and the fit function together.
210 figure;
211     plot(fdata, S11, 'or')
212     hold on;
213     plot(fdata, mdlS11(param, fdata), 'Color', 'k', 'LineWidth',
            2);
214     hold off;
215
216 % Plot the real and imaginary components of the relative
    permeability.
217 g1 = sqrt(gS1^2)*1e6*(xx/(fs1*1e9)).^(0.5);
218 g2 = sqrt(gS2^2)*1e6*(xx/(fs2*1e9)).^(0.5);
219 mu1 = 1 - ((1-(fs1./fp1).^2).*(1-(fs1*1e9./xx).^2))./((1-(fs1*1
    e9./xx).^2).^2+(g1./xx).^2)- ((1-(fs2./fp2).^2).*(1-(fs2*1e9
    ./xx).^2))./((1-(fs2*1e9./xx).^2).^2+(g2./xx).^2);
220 figure;
221 plot(xx,mu1,'--b');
222 hold on;
223
224 mu2 = ((g1./xx).*(1-(fs1./fp1).^2))./((1-(fs1*1e9./xx).^2).^2.+(
    g1./xx).^2)+((g2./xx).*(1-(fs2./fp2).^2))./((1-(fs2*1e9./xx)
    .^2).^2.+(g2./xx).^2);
225 plot(xx,mu2,'--r');
226 hold off;
227
228 % Write the best ift parameters and the best-fit |S11| curve,
    mu1, and mu2 to txt files.
229 M = [xx; mdlS11(param, xx); mu1; mu2]';
230 dlmwrite('one-loop one-gap LGR - 4 SRRs - 4 Aluminum rods - best
     fit parameters.txt', param', 'delimiter', '\t', 'precision',
     9)
231 dlmwrite('one-loop one-gap LGR - 4 SRRs - 4 Aluminum rods - best
     fit data.txt', M, 'delimiter', '\t', 'precision', 9)
```